UNIVERSIDADE ESTADUAL DE CAMPINAS

INSTITUTO DE QUÍMICA

RAPHAEL FERNANDO MORAL

PEROVSKITE MATERIALS WITH APPLICATION IN SOLAR CELLS

MATERIAIS DE PEROVSKITA COM APLICAÇÃO EM CÉLULAS SOLARES

CAMPINAS
2019

RAPHAEL FERNANDO MORAL

PEROVSKITE MATERIALS WITH APPLICATION IN SOLAR CELLS

MATERIAIS DE PEROVSKITA COM APLICAÇÃO EM CÉLULAS SOLARES

Dissertação de mestrado apresentada ao Instituto de Química da Universidade Estadual de Campinas como parte dos requisitos exigidos para a obtenção do título de Mestre em Química na área de Química Inorgânica

Master's Dissertation presented to the Institute of Chemistry of the University of Campinas as part of the requirements to obtain the title of Master in Chemistry in the area of Inorganic Chemistry

Supervisor: Profa. Dra. Ana Flávia Nogueira

O ARQUIVO DIGITAL CORRESPONDE À VERSÃO FINAL DA DISSERTAÇÃO DEFENDIDA PELO ALUNO RAPHAEL FERNANDO MORAL E ORIENTADA PELA PROFA. DRA. ANA FLÁVIA NOGUEIRA.

CAMPINAS

Ficha catalográfica
Universidade Estadual de Campinas
Biblioteca do Instituto de Química
Camila Barleta Fullin - CRB 8462

M792p

Moral, Raphael Fernando, 1990-
Perovskite materials with application in solar cells / Raphael Fernando Moral. – Campinas, SP : [s.n.], 2019.

Orientador: Ana Flavia Nogueira.
Dissertação (mestrado) – Universidade Estadual de Campinas, Instituto de Química.

1. Células solares. 2. Perovskita. 3. Materiais lamelares. I. Nogueira, Ana Flavia, 1973-. II. Universidade Estadual de Campinas. Instituto de Química. III. Título.

Informações para Biblioteca Digital

Título em outro idioma: Materiais de Perovskita com aplicação em células solares
Palavras-chave em inglês:
Solar cells
Perovskite
Layered materials
Área de concentração: Química Inorgânica
Titulação: Mestre em Química na área de Química Inorgânica
Banca examinadora:
Ana Flavia Nogueira [Orientador]
Aldo José Gorgatti Zarbin
Lázaro Aurélio Padilha Júnior
Data de defesa: 19-02-2019
Programa de Pós-Graduação: Química

Identificação e informações acadêmicas do(a) aluno(a)
- ORCID do autor: https://orcid.org/0000-0002-1844-4035
- Currículo Lattes do autor: http://lattes.cnpq.br/1774922299841872

2019

BANCA EXAMINADORA

PROFA. DRA. ANA FLAVIA NOGUEIRA

PROF. DR. ALDO JOSÉ GORGATTI ZARBIN

PROF. DR. LÁZARO AURÉLIO PADILHA JÚNIOR

A Ata da defesa assinada pelos membros da Comissão Examinadora, consta no SIGA/Sistema de Fluxo de Dissertação/Tese e na Secretaria do Programa da Unidade.

Este exemplar corresponde à redação final da Dissertação de Mestrado defendida pelo aluno Raphael Fernando Moral, aprovada pela Comissão Julgadora em 19 de fevereiro de 2019.

I dedicate this master's dissertation to my mother, Terezinha de Castro Resende, and to my departed father, Antônio Carlos Moral.

“O ser humano não é capaz de ser soberano. A soberania não está ao nosso alcance; realezas, líderes, políticos, ativistas, famosos ou figura alguma jamais o foi e jamais o será. Assim sendo, sempre nos submetemos a algo ou alguém. Ainda que alguém tenha a audácia de dizer que não se submete, essa pessoa, no seu íntimo, saberá que se submete aos seus próprios caprichos e fraquezas. Tendo dito isso, concluo que o ser humano não é livre e dificilmente será. Mas então, onde habita a liberdade?”

Acknowledgments

I want to thank God before and above anyone else, for He has always guided me and granted me a life I must always be thankful for.

I want to thank my family, especially my mother, for always supporting me in all my choices. My mom is the strongest person I have ever met, and she will always be a reference for me.

I want to thank my girlfriend, Jéssica, for always standing by my side and always believing in me; cheering me up when I am discouraged and supporting me when I am in distress. She is one of the few persons who truly know me and my inner conflicts.

I want to thank my friends for the unique experience of friendship that each of them has provided me. The list here would be long, but I wish to emphasize two names: Ana Cláudia Covaes and Felipe César Sousa e Silva. We shared many experiences during the undergraduate period, without which I would not get this far and be who I am.

I want to thank my advisor, Ana Flávia Nogueira, and her family for the opportunity of working in LNES and for receiving me in moments where my family and friends were not around.

I want to thank some remarkable professors I have had: Rogéria Rocha Gonçalves, Grégoire Jean-François Demets, Arun Timothy Royappa, Pamela Tanner, Marilda das Dores Assis, Maurício Gomes Constantino, Pearl Hong, Anne Bergan, Renata (biology in middle school), Célia Setem, Giovana (mathematics in middle school), and Marcelo Mori (SENAI). Here I think it is important to rephrase a common saying in Portuguese: “A ordem dos doutores não altera o tributo”.

I want to thank to all my dear LNES colleagues, who make the lab a nice place to work at, for all the scientific insights, and all the support that they gave me during my master’s degree.

I want to thank Douglas Soares da Silva for the TEM images.

I want to thank some people from SLAC National Accelerator Laboratory: Christopher Tassone, for his insightful thoughts and critical support; Michael Toney, for arranging everything to make my internship possible; Stephanie Moffitt, simply for being kind; Noel Hayes and Leon Leu for making my days a lot better during my internship and for the awesome friendship; Risa Benwell, for being such a nice and competent

professional; Cynthia Patty, for her smile and support always. Once again, the order here does not matter.

I want to thank some people from LNLS laboratory: Rodrigo Szostak, for letting me probe some of my samples in between his beam time; Antonio Gasperini, for the talks and insights regarding the interpretation of the data; and all the great staff that make the experiments in the beam lines possible.

I want to thank **FAPESP**, for my master's scholarship (process number 2016/02268-9);

This study was financed in part by the Coordenação de Aperfeiçoamento de Pessoal de Nível Superior - Brasil (**CAPES**) - Finance Code 001;

I also want to thank **CNPq** and all other funding agencies that contributed direct or indirectly to this work.

Finally, I want to thank everyone who, directly or indirectly, contributed to the completion of this work.

Resumo

As perovskitas de Ruddlesden-Popper, um tipo de material lamelar, são conhecidas há muito tempo, mas só recentemente esses materiais ganharam atenção especial da comunidade de optoeletrônicos. Esse ressurgimento deve-se, principalmente, a estudos recentes em perovskitas híbridas de halogeneto de chumbo que mostram um excelente potencial para conversão de energia solar. Neste trabalho, nós apresentamos um método simples para a síntese de perovskitas de Ruddlesden-Popper estáveis com fórmula geral $L_2[FAPbI_3]_{n-1}PbI_4$ (L = butilamônio ou benzilamônio; FA = formamidínio; e n = 1 ou 2). Com essa abordagem sintética, se obtém uma pasta de perovskita imprimível ou um pó, adequado para métodos de processo em solução, que são desejáveis para dispositivos optoeletrônicos. Apesar da simplicidade da síntese e estabilidade destas perovskitas, a fotoluminescência dos materiais com n=2 apresenta mudanças severas e características inesperadas. Para melhor compreender sua estrutura e comportamento fotofísico, além das técnicas espectroscópicas convencionais, foram utilizados experimentos de SAXS *in situ*, GIWAXS *in situ* e TGA. Nós demonstramos que o material à base de butilamina ($BA_2[FAPbI_3]PbI_4$) tem uma cinética de crescimento rápida e forma uma perovskita de Ruddlesden-Popper estável e de fase pura. Em contraste, devido a uma condição sintética ligeiramente mais enérgica, o material à base de benzilamina ($BLA_2[FAPbI_3]PbI_4$) parece ter uma densidade de estados de defeitos maior. Nós atribuímos essas características inesperadas de emissão à formação de poços quânticos mais espessos e a excitons auto-capturados (STE – do inglês “Self-Trapped Excitons”), originados de defeitos e modos de fônons na rede cristalina. Por fim, demonstramos a aplicabilidade desses materiais fabricando células solares: apesar do desempenho limitado, os dispositivos mostraram resultados positivos e nos deram perspectivas para trabalhos futuros.

Abstract

Ruddlesden-Popper perovskites, a type of layered material, have been known for a long time, but only recently these materials have gained special attention from the optoelectronics community. This reemergence is mainly due to recent studies in hybrid lead halide perovskites that show outstanding potential for solar energy conversion. In this work, we demonstrate a simple synthesis of stable Ruddlesden-Popper perovskite with general formula $L_2[FAPbI_3]_{n-1}PbI_4$ (L = butylammonium or benzylammonium; FA = formamidinium; and n = 1 or 2). With this synthetic approach, we obtain a printable perovskite paste or a powder suitable for solution-process methods, which are desirable for optoelectronic devices. Despite the simplicity of the synthesis and stability of these perovskites, the photoluminescence of the n=2 materials present severe changes and unexpected features. To better understand their structure and photophysical behavior, besides the conventional spectroscopic techniques, we used *in situ* SAXS, *in situ* GIWAXS, and TGA experiments. We demonstrate that the butylamine-based material ($BA_2[FAPbI_3]PbI_4$) has a fast growth kinetics and form a stable pure-phase Ruddlesden-Popper perovskite. In contrast, due to a slightly rougher synthetic condition, the benzylamine-based material ($BLA_2[FAPbI_3]PbI_4$) seems to have a higher density of defects states. We have attributed these unexpected emission features to the formation of thicker quantum-wells and to self-trapped excitons, originated from defects and phonon modes in the crystal lattice. We, then, demonstrate the applicability of these materials by fabricating solar cells: despite the limited performance, the devices showed positive outputs and gave us perspectives for future works.

Summary

1 - Introduction

1.1 - From Silicon to Perovskites

During the cold war, the USA and the Soviet Union (USSR) engaged in a dispute known as the "space race". Such competition, in a moment of political tension, was extremely meaningful, since the dominance of such resources implied in technological superiority and in a certain level of intimidation.[1] With the space race, countless scientific achievements came along, and the development of photovoltaic technologies for spacecraft is included as one of them.[2]

Although photovoltaics had critical impact in the space industry, its high cost and poor efficiency had no appeal for terrestrial applications. It was only in 1985, with a milestone of 20% efficiency of silicon-based devices, that the solar energy industry began to grow steadily and turned into an important alternative to fossil fuels. Today, with the climate change and increasingly restrictive environmental regulations, photovoltaics have become a significant solution in clean energy production, and the silicon-based applications became the dominant technology.[2]

Silicon-based solar applications are still the most cost-effective technologies in the market of solar energy.[2,3] Although the state-of-the-art silicon solar cell in laboratory overcomes 26% efficiency,[4,5] panels for large scale production are typically only 14-19% efficient.[2,6] The main cause for this discrepancy is that laboratory fabrication technics and materials are often not adequate for mass production.[2] Therefore, there remains a challenge to the scientific community to develop more cost-effective technologies for novel photovoltaics and to improve the global scenario of solar energy production.

In response to this challenge, very recently, a new paradigm in the field of solar cells has arisen: the perovskite solar cells (PSCs).[7,8] The so called organic/inorganic lead halide perovskites (LHPs) have attracted attention of scientists due to an unprecedented rise in efficiency of devices in the last 10 years. From the pioneer work of the group of Miyasaka in 2009,[9] until today, the efficiency of PSCs has increased from nearly 4% to over 24%.[10–13] Despite of the encouraging efficiency, LHPs present many drawbacks and challenges to be overcome. The following subsection is dedicated to underline these challenges based on the structure/property relationship in these materials.

1.2 - On the Lead Halide Perovskites

A LHP have the general formula $APbX_3$, where A is a monovalent inorganic/organic cation [*e.g.*, Cs^+, $[CH(NH_2)_2]^{2+}$ (formamidinium - FA), and $CH_3NH_3^+$ (methylammonium - MA)] and X is a halide (Cl^-, Br^-, I^-, or a mixture of them). The crystalline structure proper to photovoltaic applications is the same of the calcium titanate (see **Figure 1a**),[14] but several optical-inactive crystalline phases are known (**Figure 1d**).[15] In general, it is the 3D array of corner-sharing $[PbX_6]^{4-}$ octahedrons that bears the important properties for their optoelectronic applicability.[16] The optical-inactive crystalline phases, although thermodynamically more stable, do not present this 3D array of octahedrons, which generates wider-bandgap structures due to a less effective electron delocalization.[14,17]

Empirically, the size dependence of the ions to form the 3D arrays in perovskites is expressed in terms of the Goldschmidt tolerance factor (t) and the octahedral factor (μ),[18] showed in **Figure 1c** (where, r_A is the ionic radius of the cation A, r_B is the ionic radius of Pb^{2+} for LHPs, and r_X is the ionic radius of the anion X). A plot of μ vs t defines a clear cutoff where the 3D perovskite polymorphs are formed for several compositions (**Figure 1b** – highlighted square region).[16,17,19,20] The octahedral factor takes into account the coordination effectiveness of the BX_6 units, whereas the tolerance factor is related to the close-packing of the ions; in other words, the tolerance factor is a measure of the relation of the ions dimensions for a cubic or orthorhombic perovskite to form.[16] This semi-quantitative model has been initially proposed for ionic oxide perovskites (e.g., $CaTiO_3$, $SrTiO_3$, etc.) and, recently, has been adapted to LHPs.[21] Nonetheless, even with this adaptation, this model may fail to predict all (in)stable 3D perovskites, especially hybrid LHPs (*i.e.*, organic A-site cations); these deviations are associated, for instance, to the degree of covalence o the Pb—X bonding, anisotropic dipoles in organic cations, hydrogen bonding (A—X), and so forth.

There is a series of factors that, combined, make LHPs promising materials for next generation photovoltaics. Depending on the composition of these materials, regarding the cation A and the halides, they present bandgaps ranging from 1.15 eV to 3.06 eV,[22] which includes what is considered the optimal value for a p-n junction solar cell: 1.37 eV.[23] Furthermore, they show efficient charge transport for both electrons and holes,[24] and long diffusion length of the charge carriers.[25,26] The combination of the above

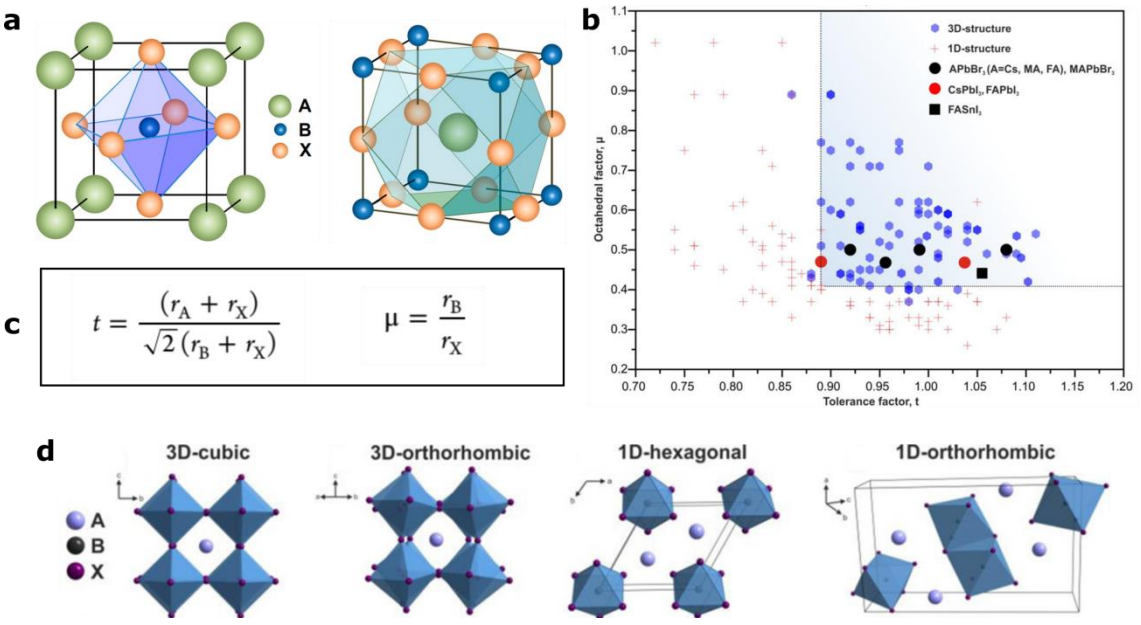

Figure 1. a) perovskite crystalline structure emphasizing the BX_6 and AX_{12} sub-lattices; **b)** plot of octahedral factor (μ) *vs* the tolerance factor (t) showing the limits where 3D perovskites are likely to form; **c)** Goldschmidt's tolerance factor and octahedral factor equations taking into account the ionic radii of A, B, and X; **d)** two 3D perovskite polymorphs and two 1D optical-inactive perovskite phases – figure adapted from references 14, 18, and 19.

mentioned properties grant perovskites outstanding potential for photovoltaic applications; in the last 10 years, LHPs gained a huge notoriety and rapidly mobilized scientists to an enormous volume of investigations known as "perovskite fever".[12]

However, with the lead-based perovskite fever, a natural question emerges: why the old villain, lead? To answer this question, we must think, first, in its closer congener elements – Sn and Ge. The first and most important difference between them is the relative stability of the bivalent cations; Pb^{2+} is much more stable than Sn^{2+} and Ge^{2+} due to relativistic effects acting on the Pb $6s^2$ electron pair.[27] In addition, the dimensional factors, μ and t, seem to be favorable for the most important LHPs compositions in room temperature.[16,20] Considering the electronic structure of LHPs, the Pb—X bonds in a 3D array result in an unusual defect-tolerant band structure. The valence band (VB) arises from the overlap between Pb^{2+} $6s^2$ and X^- np^6 orbitals, and its energy maximum has an antibonding character; whilst the conduction band (CB) is mainly composed of empty Pb $6p^0$ orbitals.[28] With this unique electronic structure, halide vacancies generate trap states that falls nearly within the VB and CB, preserving the optical and electrical features of the materials; lead vacancies are not observed, since it has the largest formation energy compared to A and X.[16] A similar bivalent cation, such as Cd^{2+} ([Kr] $4d^{10}$), would not

grant this same electronic structure, which makes Pb^{2+} very difficult to substitute. In summary, the sum of all these traits makes lead an adequate metal for perovskite-based optoelectronics, which represents an environmental challenge, given the well-known bio-toxicity of lead. Additionally, although lead presents suitable properties for LHP-based photovoltaics, the stability of these materials has also been an issue to scientists.

In spite of the rapid spike in efficiency of PSCs, the stability of this material has been the major challenge.[29–31] The main reason for this instability is the phase transition to more stable crystalline phases, induced by intrinsic chemical reactions, moisture, and UV-light.[15] To improve stability of LHPs, many strategies have been adopted: mixing cation and anion compositions,[30,32,33] incorporating polymers into/onto the perovskite films,[34,35] and applying hydrophobic layers over the solar cell,[36,37] to mention a few. A remarkable one, though, is the use of Ruddlesden-Popper 2D-layered perovskites.[38–44] The next subsection is dedicated to the structure and properties of 2D-layered perovskites and the current achievements in solar cells based in these materials.

1.3 - On the Ruddlesden-Popper Perovskites

Ruddlesden-Popper perovskites (RPPs) receive this name after the two researchers who first reported this type of material in 1957.[45,46] They consist of layered slabs of MO_6 octahedrons connected by a A—O bridge (Sr—O - **Figure 2a**). Ruddlesden-Popper Lead Halide Perovskites (RPLHPs), their analogue lead halides, have an important difference: the cation that makes the bridge is an alkylammonium with an organic backbone, **Figure 2b**; therefore, the general formula of a RPLHP may be written as $L_2[APbX_3]_{n-1}PbX_4$ (L being the organic alkylammonium bridge).[47,48] At this point, we are able to describe an important feature of the RPPs: the number of octahedron layers in each slab, denoted by "***n***" (see **Figure 2b**). Either the first RPPs or the trending RPLHPs may be visualized as an assemble of natural quantum-wells (QWs); in other words, each slab presents quantum confinement effect depending on its thickness (*i.e.*, depending on the value of *n*). This intrinsic characteristic, summed with compositional variability, endow the RPLHPs with incredible versatility.

Similarly to bulk LHPs, RPLHPs present highly compositional-dependent spectral properties. By changing the halide composition, the bandgap energy of RPLHPs varies largely within the UV-visible spectrum; also, changes in the cation A or B further shift

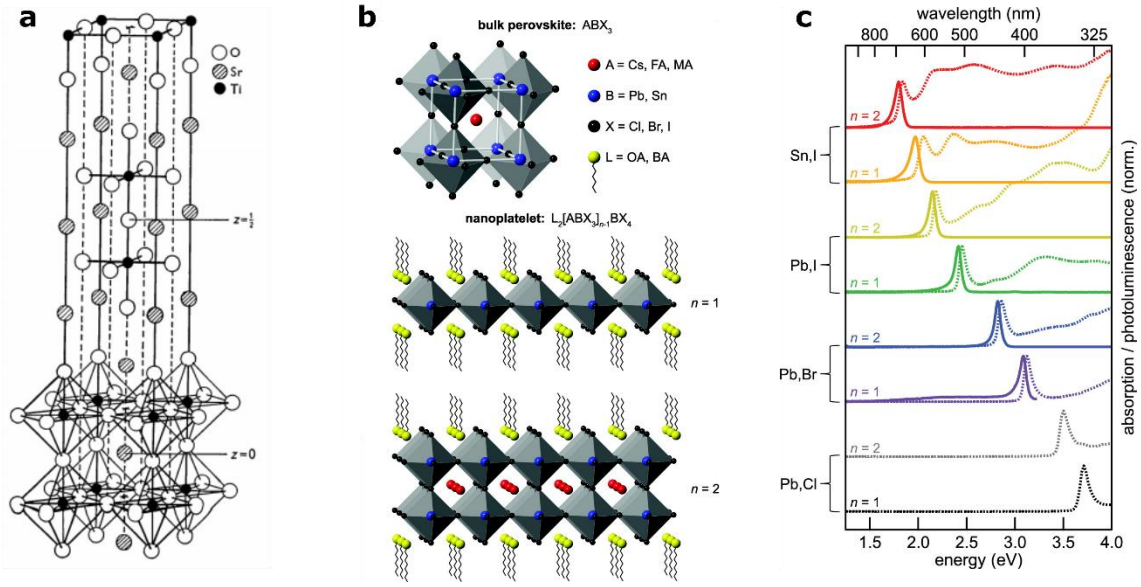

Figure 2. a) $Sr_2Ti_2O_7$ (n=2) Ruddlesden-Popper perovskite unit cell; **b)** $APbX_3$ Ruddlesden-Popper lead halide perovskites (n=1 and n=2) – observe that the cation A is different from the alkylammonium bridge (L); **c)** tunable spectral property of the RPLHPs with the composition and structure. Figure adapted from references 45 and 48.

their optical behavior (**Figure 2c**).[48] Hence, RPLHPs are especially promising due to their tunable composition and structure. Furthermore, besides this surprising tunability, the organic alkylammonium separators play a special role in their structure and properties.

The crystalline structure of the RPLHPs changes drastically with the nature of the alkylammonium cation. For instance, the lengths of the cations influence in the crystalline phases[49,50], their carbon backbones modulate their hydrophobicity[44], chromophore cationic species may improve the emission brilliance/efficiency,[51] and cations from diamines tend to yield the so called Dion-Jacobson perovskites (staggered perovskite slabs).[52,53] However, a more important effect of the organic layers in the RPLHPs is the dialectical screening of the excitons.[54–56] Excitons in RPLHPs respond to the dielectric contrast between the inorganic and organic layers, increasing their binding energy in one order of magnitude compared to the 3D perovskites (>200 meV *vs* 13-16 meV, respectively).[54,55] This additional feature in RPLHPs makes them special materials for lighting and display applications. Another remarkable contribution of the organic spacers is the improved stability that they provide compared to their 3D analogues.

To give a clear evidence of the improved stability of the layered perovskites, we shall look at the case of the $FAPbI_3$ perovskite solar cells: these solar cells are highly moisture sensitive and undergo phase transition to a yellow hexagonal crystalline phase that is optically inactive.[30] In the work of Jin-Wook Lee *et al.*, by passivating the boundaries of the perovskite grains with RPLHPs, not only an increase in stability was

observed, but also a certified stabilized efficiency of 19.77% was achieved.[40] This higher stability of the 3D $FAPbI_3$ polymorphs is due to the hydrophobicity of the organic layers, that hinders water diffusion, and also to the hydrogen bonding that the alkylammonium cations form with the halides.[49,57] Another notable example is the work of Kyung Taek Cho and collaborators, treating the surface of the active perovskite layer with a fluorinated hydrophobic ammonium salt; a layered perovskite formed on the active surface, improving its ambient stability and delivering a solar cell efficiency superior to 20%.[44] A last example of a notable work, from Sargent's group, is the direct application of RPLHPs as the active layer of solar cells. By finely controlling the QW thickness distribution using allylammonium cation layers, they fabricated a Cs/FA mixed RPLHPs (n=10 average QW thickness) solar cell with 16.5% efficiency – a significant outcome and one of the highest so far.[58]

Here, we present a simple solution-process synthesis of $L_2[FAPbI_3]_{n-1}PbI_4$; where FA = $[CH(NH2)_2]^{2+}$ - formamidinium, and L = n-butylammonium (BA = C_4H_9-NH_3^+) or benzylammonium (BLA = C_6H_5-CH_2-NH_3^+). These materials present high thermal and chemical stability and easy processability. In this work, we focused on the synthesis of the **n=1** and **n=2** materials, the understanding of their photophysics, and their potential applications in optoelectronics. For simplicity, we will denote the QW thickness of the RPLHPs in terms of **n**: <ni> (i = integer), meaning the mean QW size in a particular context. The simplicity of the synthesis and the absence of high boiling point solvents grant the easy processability of the product, which, in turn, makes it a cheap and appealing material for photonic applications.

2 - Experimental Section

Synthesis of BA_2PbI_4 (BA-1|n=1): 96.0 mg of PbI_2 (0.2 mmol), 5 mL of toluene, 1 mL o butyric acid, and 0.4 mL of butylamine are loaded in a capped flask. In a separate flask, 40.2 mg of butylammonium iodide (0.2 mmol) is dissolved in 3 mL of toluene, 1 mL of butyric acid, and 0.1 mL of butylamine. The two solutions are swiftly mixed to form an insoluble yellow solid. This solid is removed from the suspension by centrifugation at 6000 rpm for 3 minutes. The yellow pellet is redispersed in hexane and centrifuged again. The product is a bright yellow solid insoluble in nonpolar solvents.

Synthesis of $BA_2[FAPbI_3]PbI_4$ (BA-2|n=2): 96.0 mg of PbI_2 (0.2 mmol), 5 mL of toluene, 1 mL of butyric acid, and 0.5 mL of butylamine are loaded in a capped flask. In a separate flask, 20.8 mg of formamidinium acetate (0.2 mmol) is dissolved in 3 mL of toluene and 1.0 mL of butyric acid. The two solutions are swiftly mixed to give an insoluble red solid. This solid is removed from the suspension by centrifugation at 6000 rpm for 3 minutes. To obtain a dry solid, the red pellet is redispersed in hexane and centrifuged again. A paste, useful for printable layers, can be obtained by redispersing the pellet in toluene and centrifuging it again, resulting in a red paste.

Synthesis of $BLA_2[FAPbI_3]PbI_4$ (BLA-2|n=2): 96.0 mg of PbI_2 (0.2 mmol), 5 mL of toluene, 1 mL o butyric acid, and 0.5 mL of benzylamine are loaded in a capped flask. In a separate flask, 20.8 mg of formamidinium acetate (0.2 mmol) is dissolved in 3 mL of toluene and 1.0 mL of butyric acid. The two solutions are swiftly mixed to give an insoluble dark brown solid. This coarse suspension is heated to a mild temperature (70 °C), and the color slowly changes from dark brown to dark red: when it turns to a brighter red, characteristic of a <n2> RPLHP, the suspension is quickly cooled in water bath, otherwise the solid is redissolved. The final red product is removed from the suspension by centrifugation at 6000 rpm for 3 minutes. To obtain a dry solid, the pellet is redispersed in hexane and centrifuged again. A paste, useful for printable layers, can be obtained by redispersing the pellet in toluene and centrifuging it again, resulting in a red paste.

Blade-coat films preparation: a paste of the materials BA-2 or BLA-2, obtained as described above, is deposited on the edge of a glass substrate fixed on a bench with a tape. With the help of a Pasteur pipette, the paste is carefully spread over the glass surface and allowed to dry, yielding a thick and smooth film.

Thin film preparation: thin films of BA_2PbI_4 are prepared *via* spin-coating. The solid material is dissolved in anhydrous acetonitrile in the desired concentration, and the solution is spin-coated at 1000 rpm for 30 s and 3000 rpm for 10 seconds. The same procedure is followed to prepare $BA_2[FAPbI_3]PbI_4$ thin films, but its solutions can be either in tetrahydrofuran or acetonitrile. Acetone also dissolves both materials, but the visual quality of the films is inferior.

Absorption spectra: absorbance in thin films was measured in an Agilent Carry 60 UV-vis equipment in transmission mode. A glass substrate was used as the baseline for all the spectra.

Diffuse reflectance spectra: spectra were measured in a Shimadzu UV 2450 equipment. The materials were spread onto glass and allowed to dry, so their reflectance spectra were measured from the powder.

Photoluminescence spectra and emission surfaces: spectra were collected in a Horiba Fluorolog-3 on the blade-coated films. The excitation source was perpendicular to the film, and the emission was collected at an angle of approximately 15°. Data were corrected according the lamp and detector fluctuations (xenon lamp) with correction algorithms from the equipment software. Same procedure was followed for thin film analysis.

Time resolved photoluminescence: the decay curves were measured in an Edinburg Instruments nF900. These measurements were carried out on the blade-coated films of the powder materials with a pulsed laser of 375 nm. The detector used in the measurements was a single-photon-counter with 2048 channels.

X-ray diffraction: diffractograms were registered in a Shimadzu XRD-7000 with a Cu Kα source (1.54 Å). The scanning step was 0.05 2θ° with 4 seconds of integration (6 seconds integration for BA_2PbI_4 - <n1>).

Synchrotron Small Angle X-ray Scattering (SAXS): these experiments were performed in SSRL ring – beam line 1-5 – in SLAC National Laboratory, a division of Stanford University. The formation kinetics of $BA_2[FAPbI_3]PbI_4$ were studied by probing the reaction *in situ* with a beam energy of 15 keV. With an inline reactor flask, the reaction was run as described in the procedure above. Data collection started a few seconds before and after the mixture of the FA solution, comprising a total time of 30 s. The exposure time of each collection was only 100 ms, given the velocity of the reaction. After this 30 s, the reaction was allowed to age, collecting SAXS data with 5 s exposure time with 1 s sleeping time. The 2D images were converted to 1D scattering curves by integrating them radially with respect to the beam center; the integration is a representative collection of the scattering in all directions, considering an isotropic scattering. The detectors used in the experiments were either a Dectrix Pilatus-300 or a Dectrix Eiger. For an overview of the principles of this technique, the reader may consult the appendix.

Synchrotron Grazing Incidence Wide Angle X-ray Scattering (GIWAXS): GIWAXS data were collected at LNLS laboratory in CNPEM facility at the beam line XRD2 with beam energy of 8 keV. The angle of incidence was 3°, exposure time of 5 s, sleep time 25 s. The detector used was a Dectrix Pilatus-300: all the data collected were normalized to compensate the decrease in the synchrotron ring current over time. Every

image from the area detector was converted to a 1D diffractogram; these diffractograms were put together to build a 2D map resolved in time. An overview of the principles of this technique is also available in the appendix.

Transmission electron microscopy (TEM): images were collected in a Zeiss Libra 120 operating at 80 keV. Samples were prepared by suspending fine particles of the solid in hexane and drop-casting them onto a TEM grid.

Thermogravimetric analysis (TGA): the measurements were made in a TA instruments – TGA 2050 in alumina crucibles with the sample powders BA-2 and BLA-2. Data were collected in inert (Ar) and oxidant atmosphere (synthetic air). The heating speed of the equipment was 10 °C/min and the temperature range was from 30 – 600 °C.

3 - Results and Discussion

3.1 – Synthesis

In summary, this synthetic approach relies on the large excess of alkylammonium cations over the other components (~25 fold). To guarantee the formation of the alkylammonium species, we use a ratio of 4:1 of butyric acid/butylamine (for detailed information, see the experimental section). This excess of alkylammonium is a key factor for anisotropic growth,[19,59] although a precise mechanism for this growth is yet to be elucidated. In this work, we were able to cast some light into the formation mechanism of BA-2 *via in situ* small angle X-ray scattering analysis (SAXS), which we shall discuss below.

The first remarkable point to address regarding the synthesis of the n=2 materials is that BA-2 is readily formed upon the mixture of the two precursor solutions, whereas the BLA-2 requires temperature to form. A consistent explanation for this observation is that during the formation of BLA-2, benzylammonium cations offer a barrier for the perovskite layers to form, leading to a bulk-like material of dark brown color. Upon gentle heat (70 °C), this brown solid slowly turns into a vivid red color, identical to its relative BA-2 (**Scheme 1a**). On the contrary, when using butylammonium, the formation of a layered perovskite is virtually instantaneous, even at room temperature. SAXS data demonstrate this fast kinetics of the BA-2 reaction and its phase purity, **Figure 3**. These

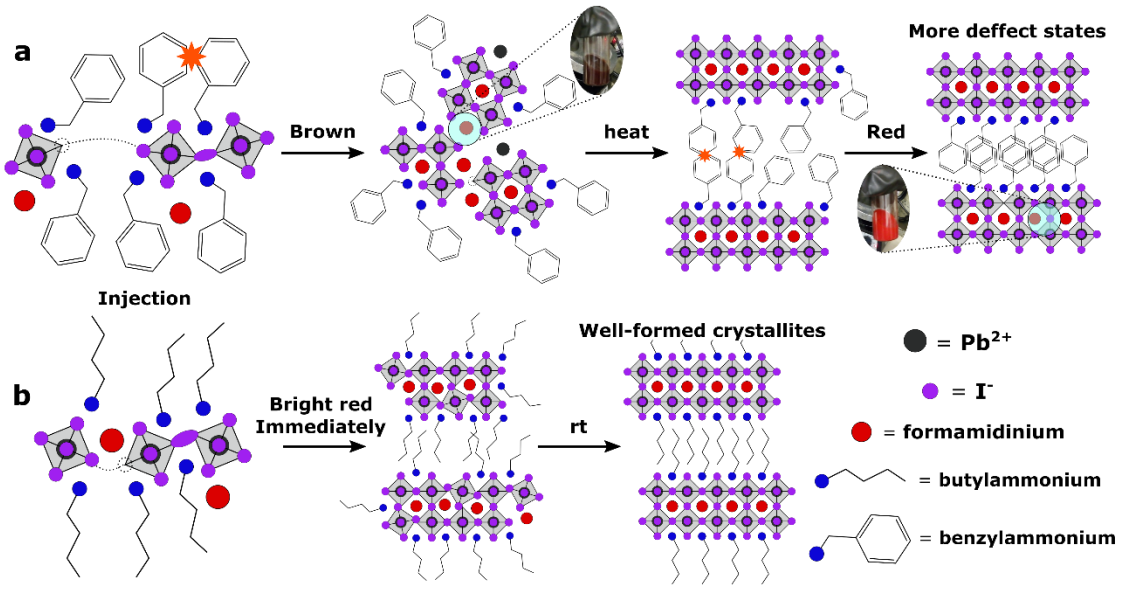

Scheme 1. Schematic mechanism of formation of **a)** BLA-2 and **b)** BA-2.

observations also help explain the spectral differences between these similar materials, which will be discussed later in this text.

From **Figure 3a**, we see a rapid spike in the scattering intensity showing the growth of nano-sized materials. More quantitatively, **Figure 3b** shows that, within the first 10 seconds of reaction, the layers of perovskite start to self-assemble into a crystal lattice, as can be inferred from the broad diffraction in ~0.29 $Å^{-1}$ (cyan curve). Concomitantly, the scattering intensity coming from the precursors, at higher Q values (>0.1 $Å^{-1}$), decreases continuously along the first 30 s of reaction, which suggests that the slabs continue to grow while assembling into a RPLHP. **Figure 3c** and **d** show the full evolution of the diffraction peak from the [00l] direction. In summary, although the BA-2 material continues to grow until 40 minutes of reaction, its growth kinetics is quick, forming a phase-pure material.

Unfortunately, we could not perform the same experiment for the BLA-2 reaction using SAXS, which would provide insightful information to better compare the two materials and their (different) properties. These SAXS data for the BA-2 reaction supports what we suggested in the **Scheme 1b**. The indirect formation of BLA-2, summed with the need of heat, certainly causes the material a higher density of defects, which influences in its photophysics, as we shall discuss herein. Moreover, we cannot assume phase purity for BLA-2, since we do not have the single crystals reference nor the SAXS curves for this material. Having considered these facts, we address that further

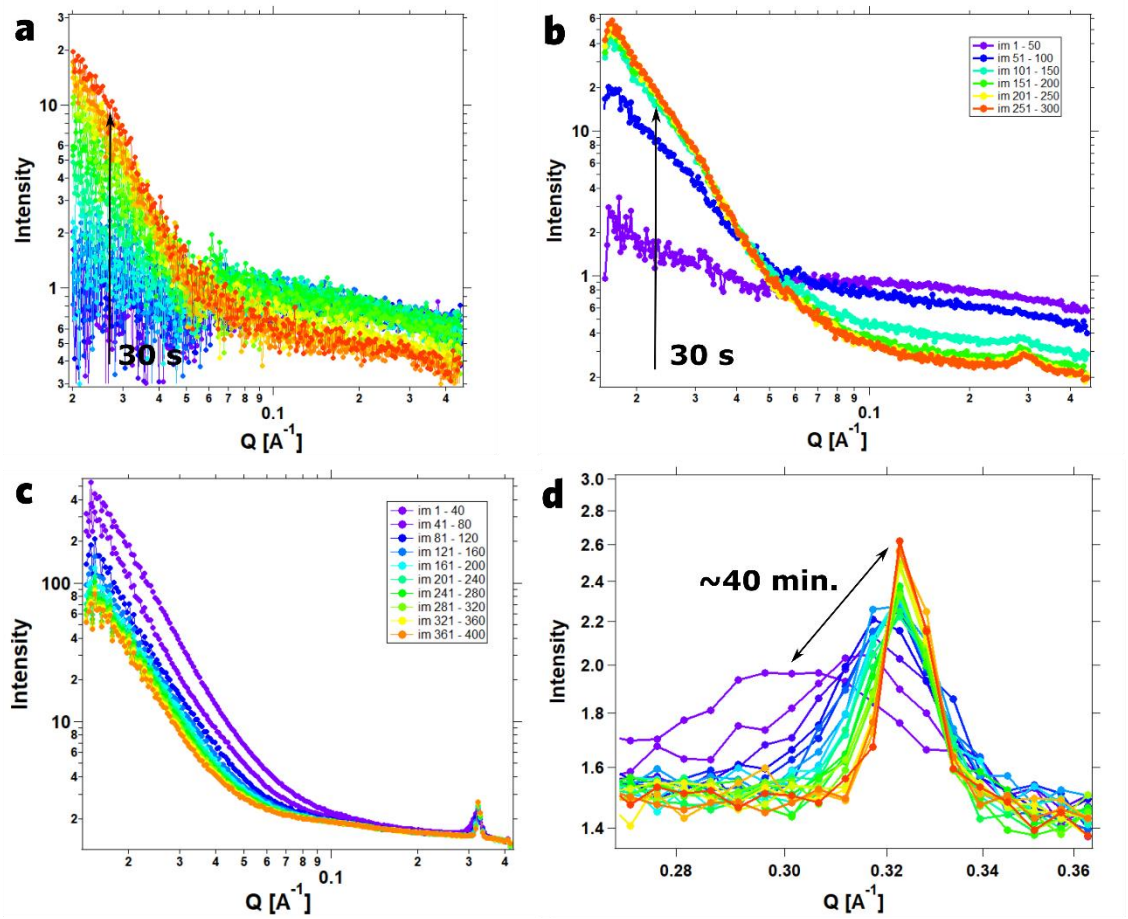

Figure 3. SAXS data from the formation reaction of BA-2 material **a)** first 30 seconds of reaction as it takes place with each curve corresponding to 0.5 second – collection started a little before FA solution injection; **b)** same initial 30 seconds with each curve corresponding to 5 seconds; **c)** aging experiment right after the initial 30 seconds – each collection had 5 seconds of exposure time; **d)** same diffraction evolution from **c** emphasized – the total time lapse of the aging experiment was about 40 minutes.

investigation is necessary to better understand and optimize the synthetic conditions of BLA-2.

A last information extracted from SAXS data is the diffraction peak shifting from 0.29 $Å^{-1}$ to 0.32 $Å^{-1}$. This shift indicates that the distances between the {00l} planes are larger initially, which can be due to solvent trapping between the layers. This observation is particularly important when considering BLA-2 synthesis; since it forms slowly than BA-2, solvent trapping is even more likely in this material. Thermogravimetric analysis (TGA) confirmed the presence of a small volatile fraction in BLA-2 sample (see subsection **Structure to Properties Relationship**). Finally, for the formation of BA-1 material, although we do not have SAXS data for its reaction, we expect a similar behavior to its analogue BA-2 with no further complications.

3.2 - Structural Characterization

The X-ray diffraction (XRD) patterns for BA-1, BA-2, and BLA-2 materials are depicted in **Figure 4d**, **e**, and **f**, respectively, along with the illustration of their crystalline structure – **Figure 4a**, **b**, and **c**. In the XRD of BA-1, we can clearly observe a preferential orientation along the [00l] direction: this material, even in the form of a fine powder, apparently gets easily oriented due to its sheet-like crystals. The less intense diffractions are not easily observed in the experimental diffractogram because their intensities are low and comparable to the baseline noise. For the BA-2 powder, the XRD pattern, disregarding the intensities, agrees with the single crystal reference.

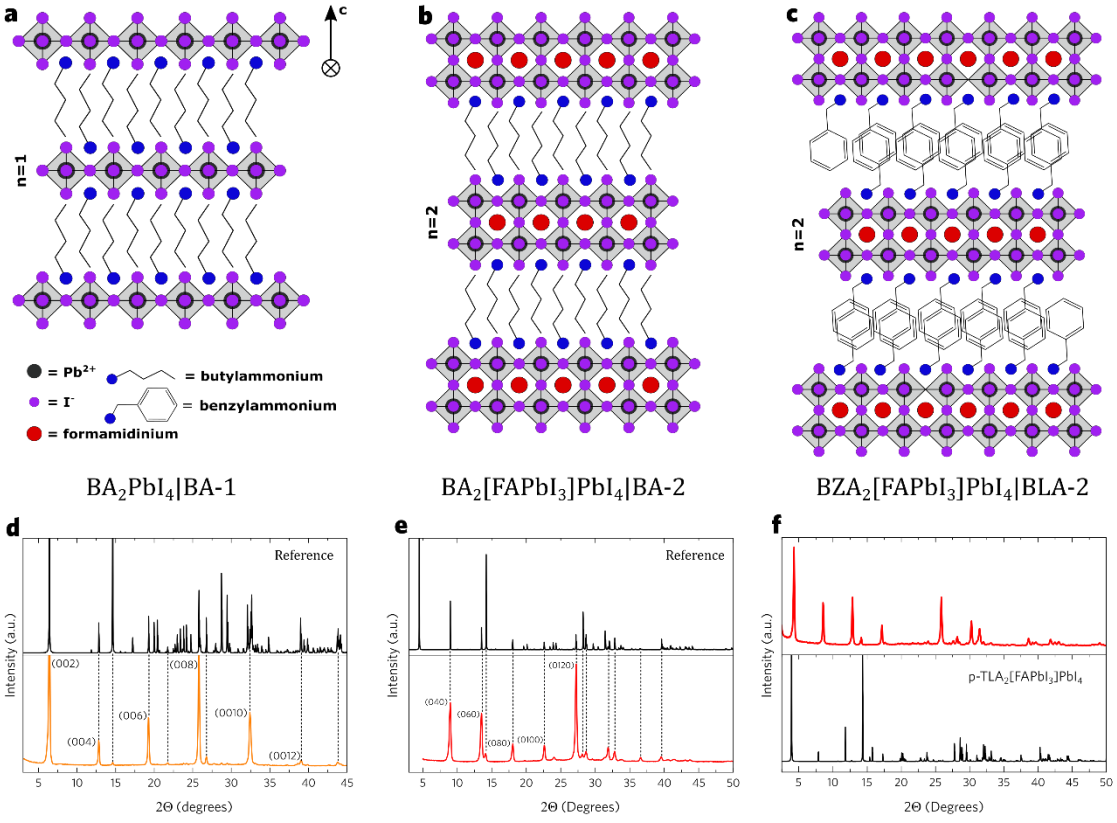

Figure 4. a) schematic representation of the crystal structure of the BA-1; **b)** schematic representation of the crystal structure of the BA-2; **c)** schematic representation of the crystal structure of the BLA-2; **d)** XRD pattern of the BA-1 powder; **e)** XRD pattern of BA-2 powder; and **f)** XRD pattern of the BLA-2 powder compared to a similar material – the references in **b** and **c** were calculate from the single crystal data available in the literature.

The single crystal reference used for BA-2 was its analogue with methylammonium (MA).[47] From the single crystal XRD data of BA_2[**MA**PbI_3]PbI_4, we simulated the powder X-ray diffraction for $BA_2[FAPbI_3]PbI_4$, since their point group

(Cc2m) and lattice dimensions are the same. The peak positions in the resulting simulated diffractogram agree perfectly with the experimental data. However, similarly to the BA-1, BA-2 may also get oriented when pressing its powder against the sample holder, which would generate unexpected intensity spikes of some higher order Bragg reflections. Lastly, no unexpected diffractions were observed in both experimental diffractograms (BA-1 and BA-2), leading us to conclude that the materials present phase purity.

To the best of our knowledge, the single crystal XRD diffraction of $BLA_2[FAPbI_3]PbI_4$ has not been reported up to now, which suggests that we have prepared a novel RPLHP. Since we could not grow a single crystal of this material yet, we have compared our powder X-ray diffraction to a related structure: the *p*-toluidine analogue (*p*-$TLA_2[FAPbI_3]PbI_4$),[60] and both XRD diffractions are depicted in **Figure 4f**. Here we have to establish some boundary conditions: 1) these structures present highly intense peaks in low diffraction angles, due to the large dimension of the unit cell along the [00l] direction; 2) the methyl group in *p*-toluidine should not change drastically the unit cell dimensions compared to benzylamine; and 3) there is a common diffraction at approximately 25 2Θ for all the three materials reported in this work, BA-1, BA-2, and BLA-2. Therefore, given the abovementioned approximations, the similarity of the diffractograms in **Figure 4f** suggests that we indeed obtained the RPLHP with *n*=2, BLA-2, as expected. Also, the position of the excitonic emission (see subsection "**Optical Characterization**") agrees with its butylammonium analogue.

To further investigate the composition of these materials, we collected the Fourier-Transform Infrared (FTIR) spectra of the powders, **Figure 5**. The butylammonium RPLHPs present the absorption signature of alkylammonium compounds: N-H and C-H stretching/bending vibrational modes. Since the chemical environment of N-H bonds in BA-1 and BA-2 are different (space group Pbca and Cc2m, respectively), their vibrational modes in FTIR might be different; also, formamidinium cations present in BA-2 have two NH_2 groups that will absorb in this region as well.[61] Interestingly, BA-2 FTIR still shows a clear carbonyl absorption of butyric acid (ν=1710 cm^{-1} C=O), which shows that butyric acid is still present in the BA-2 material (most likely weakly bonded to the surface, as suggested for analogue materials).[62] After the synthesis, the material still presents the characteristic smell of butyric acid that fades with time without degrading the powder; this observation indicates that butyric acid is only weakly bonded to the surface. At last, a critical difference between BA-1 and BA-2 FTIR spectra is the formamidinium broad band in 607 cm^{-1}, **Figure 4a**.[63]

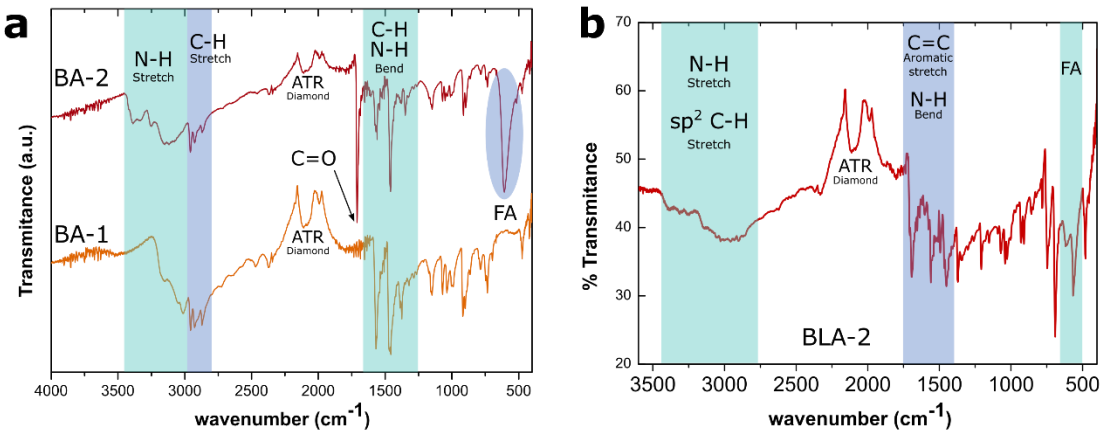

Figure 5. a) Attenuated Total Reflectance (ATR) infrared spectra of BA-1 and BA-2; and **b)** ATR infrared spectra of BLA-2 material.

BLA-2 material presents many differences in the FTIR spectrum compared to the butylammonium counterparts (**Figure 5b**). The N-H stretching modes are visible, but they overlap with sp^2 C-H stretch, forming a broad absorption band between 3500-2900 cm^{-1}. The C=C stretching and N-H bending modes overlap in the region between 1500 to 1700 cm^{-1}. Two vibrational modes of the aromatic ring are observed in the region from 690 to 790 cm^{-1}, revealing the mono-substituted ring vibration pattern. Lastly, similarly to BA-2, the absorption of the FA cation is also observed in 609 cm^{-1}.[63]

We attempted to take some TEM pictures of the materials with little success. Since the solids cannot be dispersed in non-polar solvents, getting a fine suspension of them was extremely dispendious. We tried to prepare TEM samples of BA-1 and BA-2, suspending them in hexane or toluene, but the results were not encouraging; they showed either undistinguishable agglomerates of large particles or agglomerates of fine fragments. **Figure 6** shows the best TEM images taken from the BA-2 solid.

The important feature revealed by the TEM images is the plaque format of the crystals. In the right picture we observe sharp edges of the plaques with areas of thousands of nm^2, which is expected for this type of material. Surrounding the plaques, the needle-like crystals are most likely formed by butylammonium butyrate remaining from the synthesis, as observed in the FTIR, and small fragments of the material. Having presented the structural characteristics of the products, in the following section we shall present their optical characterization and discuss its intriguing behavior.

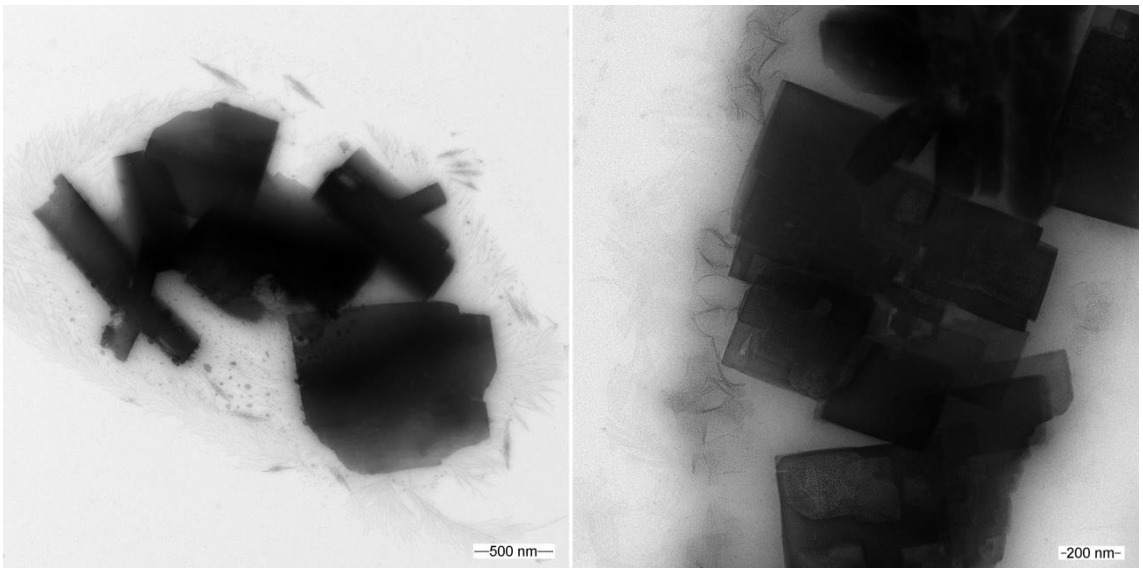

Figure 6. TEM images of BA-2 material showing its plaque-like crystal structure.

3.3 - Optical Characterization

$BA_2[FAPbI_3]PbI_4$ (n=2) powder has an emission that is not perceptible to the naked eye (emission maxima at 579 nm and 609 nm, **Figure 7b**). Although insoluble in toluene, this red product forms a paste with this solvent that can be used as an ink. This ink is totally printable and can be blade-coated onto a glass substrate to form a smooth film (**Appendix Figure 1**). This film is stable in ambient atmosphere and can be thermally treated up to 120 °C without degrading the 2D-perovskite crystalline phase. Nonetheless, it suffers a change in the emission overtime that will be further discussed herein. $BLA_2[FAPbI_3]PbI_4$ is very similar to its butylammonium counterpart (**Figure 6c** - emission maxima at 581 nm and 596 nm). Their QW thickness is the same, and so is the extent of their quantum confinement, which, *a priori*, gives them similar spectral properties.

Their differences appear when considering the different nature of the organic separators: the dielectric contrast between perovskite/butylammonium is higher when compared to perovskite/benzylammonium, and this structural difference leads to a different level of dielectric screening. This phenomenon influences directly in the exciton binding energy and, therefore, corresponding shifts in the absorption and emission spectra are observed.[55,56]

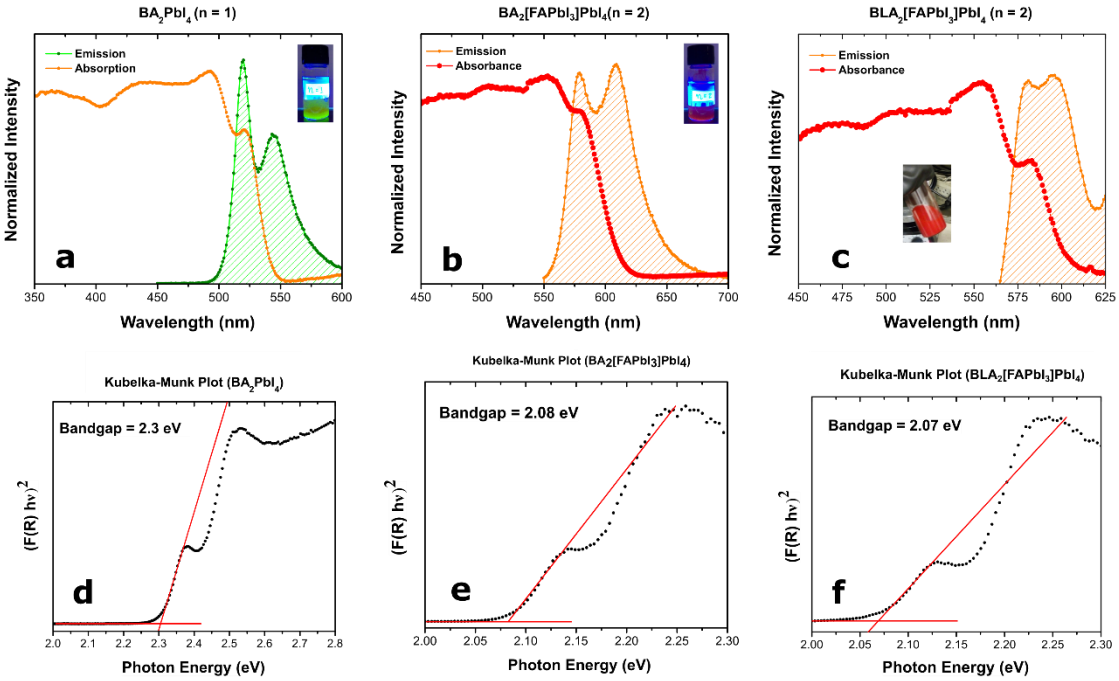

Figure 7. **a)** – **c)** Absorption and emission spectra of the three RPLHPs and **d)** – **f)** their respective Kubelka-Munk/Tauc plots with bandgap estimation at the intersection of the linear fit and the base line (red lines) – the inserts in **a** and **b** are the materials under UV-light, and the insert in **c** is the material as synthesized.

BA_2PbI_4 (n=1) powder is bright yellow and has an intense green emission, perceptible even under ambient light (emission maxima 520 nm and 545 nm – **Figure 7a**). Unlike $BA_2[FAPbI_3]PbI_4$ and $BLA_2[FAPbI_3]PbI_4$, this yellow product is not prone to form a paste with toluene. For this reason, this material is not as "printable" as its analogues (see **Appendix Figure 2**). Once this material is washed and dried, it is stable under ambient atmosphere and its green emission does not change over time. Lastly, **Figures 7d** – **f** show the respective Kubelk-Munk/Tauc plots of the three materials. The optical bandgap (E_{go}) of the materials is estimated where the linear fit of the straight region of the absorption edge meets the base line of absorption;[64,65] the values found for E_{go} are in agreement with the literature.[47]

We observed that, overtime, the films of $BA_2[FAPbI_3]PbI_4$ present modifications in the photoluminescence (PL): the excitonic emission loses intensity while other emissions appear (**Figure 8a** and **b**). This change is completed with an emission that is closer to bulk $FAPbI_3$ perovskite in 750 nm, **Figure 8c**. This process is accelerated by illumination, especially with UV light, as observed in **Figure 8d**. We suppose that UV light induces butylamine and HI evaporation, similarly to degradation mechanisms proposed to methylammonium LHPs.[66] An overall reaction can be written for this process with $BA_2[FAPbI_3]PbI_4$ as a starting material.

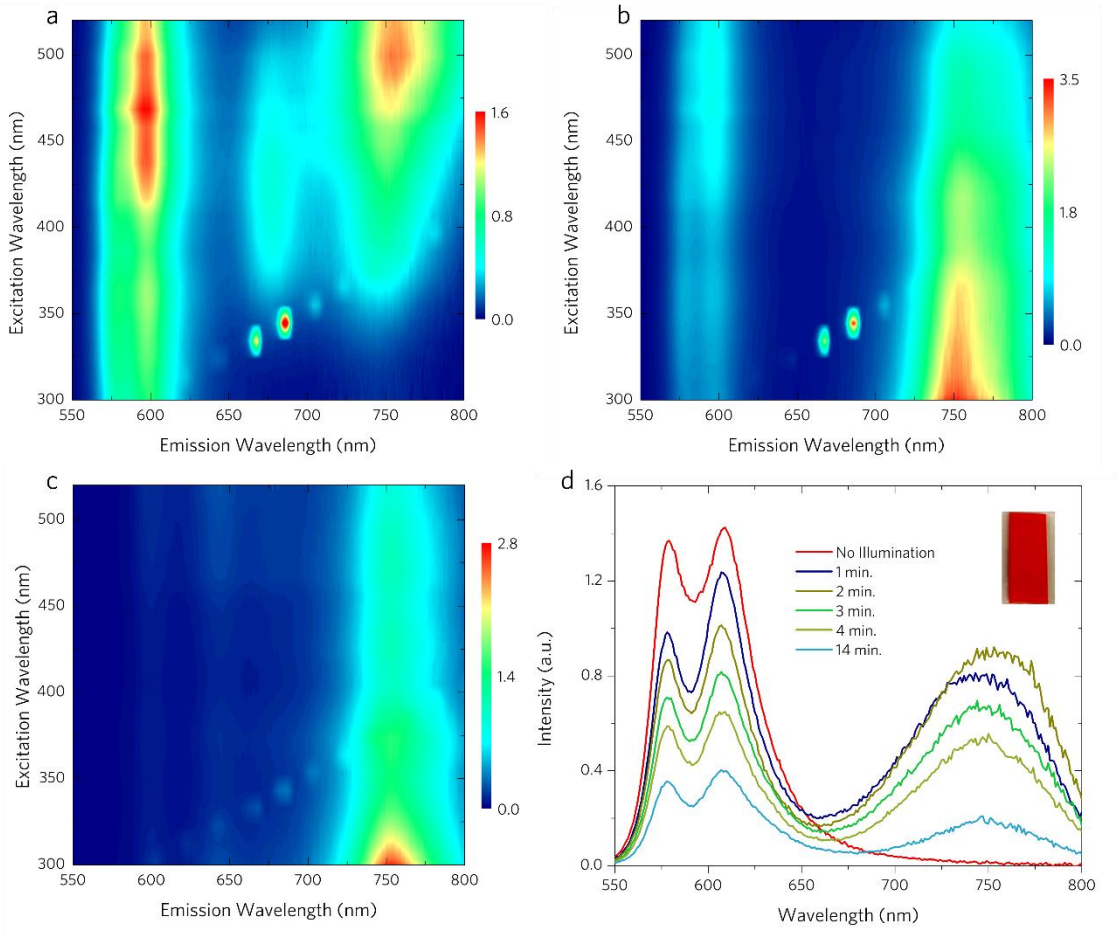

Figure 8. Excitation *vs* emission spectra of the $BA_2[FAPbI_3]PbI_4$ blade-coated film **a)** first surface after film fabrication; **b)** second surface half an hour later using the same film; **c)** third surface after a couple days with the same film; and **d)** fresh film emission spectra at 405 nm excitation before illumination and after several illumination times – the insert is a blade-coated film of the material onto glass. The dot signals describing a diagonal in **a**, **b**, and **c** are scattering artefacts.

$$\mathbf{a}\ (RNH_3)_2[FAPbI_3]PbI_4 \rightarrow \mathbf{X_a}RNH_{2(g)} + \mathbf{X_a}HI_{(g)} + (\mathbf{a-1})\ PbI_2 + (RNH_3)_2[FAPbI_3]_{\mathbf{a}}PbI_4$$

In the equation above, $\mathbf{X_a = 2a - 2}$ and **R** = butyl. This equation simply shows that, if **a**=2, for instance, the final product will be a thicker QW with *n* = a+1; in other words, if two moles of starting material <n2> reacts according to the reaction above, a <n3>-QW will form along with amine, HI, and PbI_2 (the reader may understand better sketching this reaction with different values of **a**). These thicker QWs have lower bandgap energy that can trap charges; that is, the domains of different QW thickness generate an energy cascade where charges are transferred from the wider bandgap domains to the narrower ones.[58,67,68] This charge transport could be one of the causes for the fast quench observed in **Figure 8d**. After several days, or intense heat treatment, the films darken, which corroborates to the hypothesis of thicker perovskite QW domains (see **Appendix**

Figure 3). Moreover, amine loss increases the density of defects, which may also influence in the emission. In summary, both the structural defects and the thicker QW domains may be the reason for the PL anomalies observed in **Figure 8**.

While BA-2 material initially may not show any emission rather than the excitonic one (**Figure 8d** – black curve), BLA-2 analogue shows several emission bands, even when freshly synthesized (see **Figure 9b**). In order to better compare and discuss these unexpected emission behaviors, their general spectral changes are depicted in **Figure 9**. The difference in the relative intensities in the BLA-2 emission is expected, since the synthetic condition for this solid is rougher (mild heat). The origin of the broad emissions around 750 nm in both materials is most likely trap emissive states (defects), as strongly suggested by their respective photoluminescence excitation (PLE) spectra (**Figure 9a** and **b**). Both PLE spectra show a clear excitonic peak (566 nm for BA-2 and 568 nm for BLA-2), meaning that the excited electrons are transferred to lower energy states before emission.

In the literature, there is an agreement that this emission broadening comes from both inhomogeneous broadening (defects) and exciton-phonon coupling. A common used model to elucidate this phenomenon is the following:[69,70]

$$\Gamma(T) = \Gamma_0 + \Gamma_{phonon}\left(e^{E_{LO}/k_BT} - 1\right)^{-1} + \Gamma_{inhomo}(e^{-E_b/k_BT})$$

where Γ_0 is the full width at half maximum (FWHM) of the target emission band at 0 K (an extrapolation), Γ_{phonon} is the coupling constant of the exciton with the longitudinal-phonon (LO), E_{LO} is the energy of the LO, Γ_{inhomo} is the inhomogeneous broadening coefficient, E_b is the average binding energy of defect emissive states, k_B is the Boltzmann constant, and T is the temperature. A plot of the FWHM of the target emission *vs* the temperature produces a curve that can be modeled by the equation above; then, E_{Lo} may be directly compared to phonon frequencies in Raman spectroscopy. Emma *et al.*[69] and Krishnamoorthy *et al.*[70] have found E_{LO} values that agree with both inorganic and organic centered phonon frequencies. The combination of efficient exciton-phonon coupling and emissive defect states generate a broad energy distribution of emissive states, commonly attributed to self-trapped excitons (STE).[56,69–73] As it is written in the review work of Kagan's group: "Strong exciton−phonon coupling and the 'softness' of the perovskite metal-halide framework and the organic cations, particularly as their fraction increases in

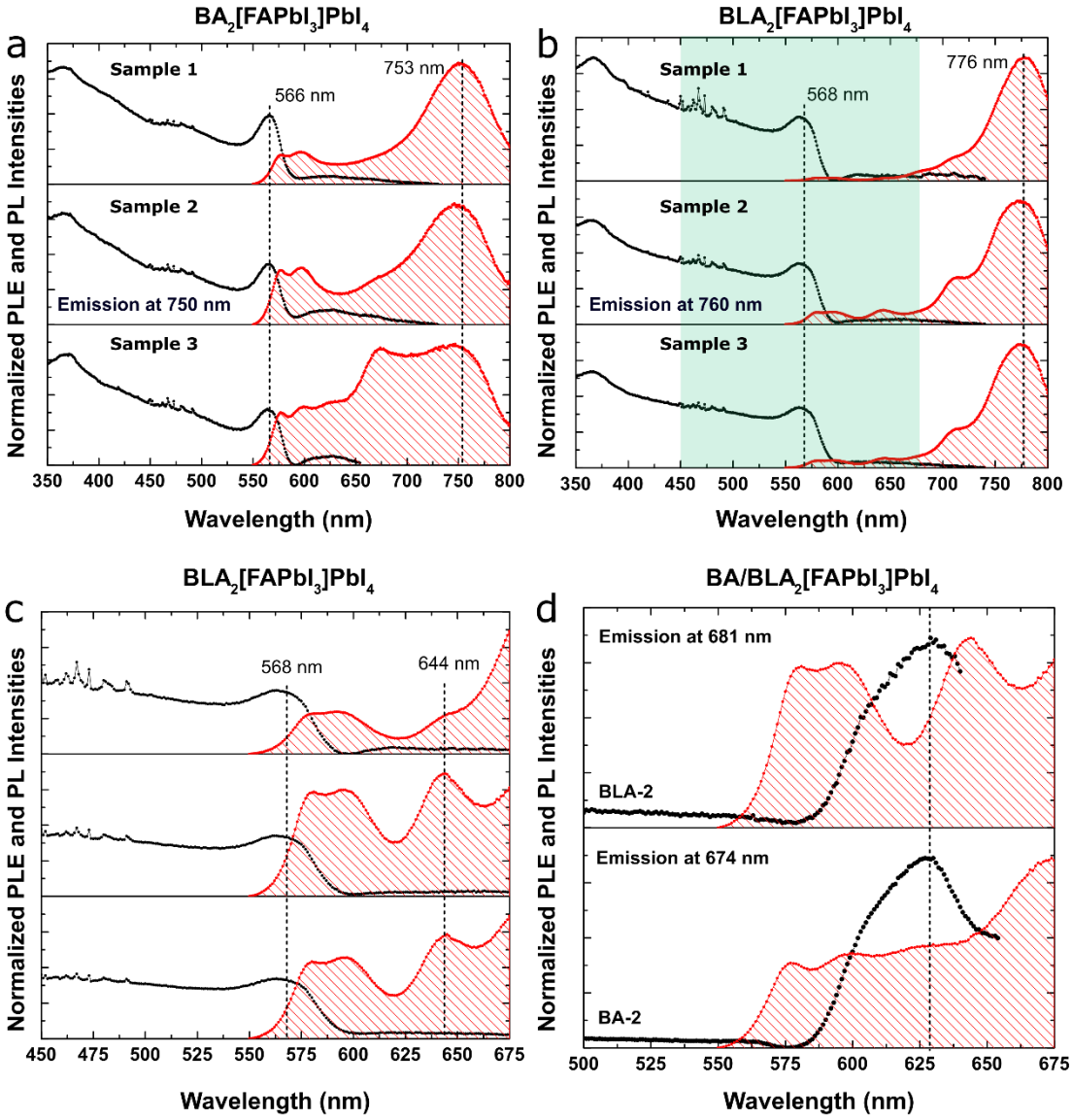

Figure 9. Three distinct photoluminescence excitation and emission spectra of BA-2 and BLA-2 after aging the samples in ambient atmosphere and ambient light – all the emissions (red filled curves) were collected with 405 nm excitation – **a)** three BA-2 PLE spectra (collected at 750 nm) along with their respective emissions; **b)** three BLA-2 PLE spectra (collected at 760 nm) along with their respective emissions; **c)** Amplification of the rectangle highlighted in **b**, with normalized intensities, for clarity; and **d)** excitation spectra of BA-2 and BLA-2 at 674 nm and 681 nm emission wavelengths, respectively.

2D perovskites, set up the conditions for self-trapping".[56] Given the large amounts of works in the literature claiming that the broadening in the emission of RPLHPs is due to STE, we conclude that we are very likely to be observing the same phenomenon. Nonetheless, to complete the assignment of these emissive features, we must consider the hypothesis of other QW domains.

In the **Figure 9d**, we observe a different energy level detected when the PLE spectra are collected from intermediary emission maxima (674 nm for BA-2 and 681 nm

for BLA-2). This unexpected energy level supports the hypothesis of other QW domains such as <n3> or <n4>, most likely <n3> because of the energy match with this crystalline phase.[47] However, this energy level does not have the profile of a semiconductor that absorbs all the energies above the bandgap, which inserts an extra complication to simple assign this peak as a thicker QW energy level. Therefore, the PLE spectra alone are not conclusive for this hypothesis.

With all the discussion we have made so far, we are able to have a broader comprehension of the emission of these materials: besides the excitonic emissions, we have bands that are likely to come from other QW phases and a broad band that is likely to emerge from STE. At last, **Figure 9c** is a magnification of the region highlighted in blue, in **Figure 9b**, with normalized intensities; this amplification allows us to compare the differences in the excitonic emissions of BA-2 and BLA-2. As mentioned before, this variance emerges from the different levels of dielectric screening and also from lattice distortions particularly induced by each species of alkylammonium cation.[49,74]

3.4 - Optical Characterization of the Thin Films

So far, we have discussed the optical properties related to the solid powder deposited on glass films *via* blade-coating. Nonetheless, the thin films of these materials present significant optical changes. **Figure 10** depicts their absorption and emission spectra. Different from the absorbance obtained from the reflectance, the spectra taken from the transmittance show more accurately their quantum-confinement effect with a sharp excitonic absorption. These sharp peaks reflect a highly confined system, generating well-defined electronic states (excitons).

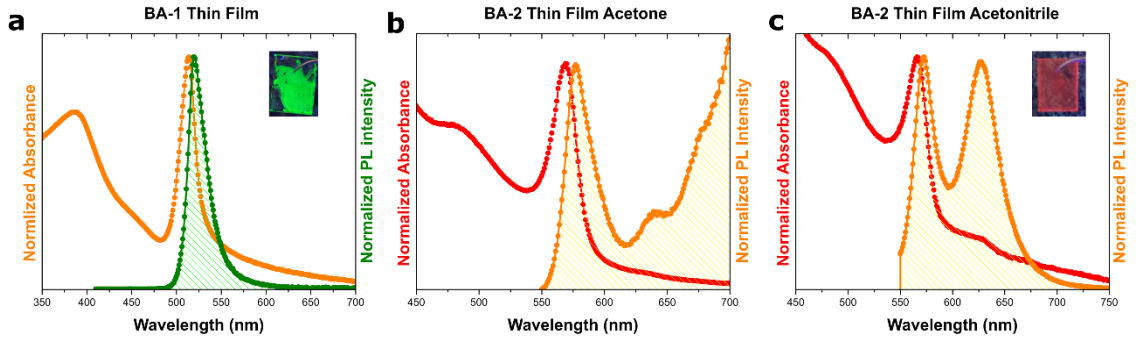

Figure 10. Absorption and PL spectra of BA-1 and BA-2 thin films **a)** spectra of BA-1 thin film on glass prepared with solution in acetonitrile – the insert is a picture of a film under UV-light; **b)** spectra of BA-2 thin film on glass prepared with solution in acetone; **c)** spectra of BA-2 thin film on glass prepared with solution in acetonitrile – the insert is a picture of a film under UV-light.

Figure 10a shows the absorption and emission spectra of a BA-1 thin film on glass. This highly emissive film shows very similar optical properties to the powder and a small Stokes shift. However, the emission from the thin film does not have the broader second band seen in **Figure 7a** (545 nm). This behavior is far from trivial, and very little reports in the literature talk about it. Mitzi, in his report on BA_2MI_4 ($M = Pb^{2+}$, Sn^{2+}, and Ge^{2+}),[75] shows the PL from a single crystal of BA_2PbI_4 (BA-1) with exactly the same features observed in **Figure 7a**. In the report, the author says that this feature is probably a result of oxidation and ambient degradation. We, however, suggest that this feature may appear with the degree of packing of the slabs: this hypothesis would explain why the powder and the monocrystal show this second band, whereas the thin film does not. This lower energy emission may be a result of multibody interactions, as the degree of stacking in the powder is higher than in thin films.[76] In other words, because the thin films have a much lower number of overlapping slabs, this broad emission is not observed. In the work of Jasmina *et al.*,[77] they reported that an accurate model to calculate the bandgap in RPLHPs has to take into account the extension of the hole/electron wave functions to outside of the slabs, which happen to overlap, forming minibands.[78] This work reinforces the hypothesis that the degree of stacking influences in the electronic properties of RPLHPs; however, this supposition is merely speculative and the PL lifetime decay of the powder BA-1 material suggests that, instead of minibands, we might be observing electron-phonon interactions, as we discuss in the following paragraphs.

Figures 10b and **10c** show the absorption and emission spectra of BA-2 thin films prepared with acetone and acetonitrile solutions, respectively. The acetone film had poorer quality than the acetonitrile film, most likely because acetone was not anhydrous. Consequently, the film from acetone solution shows very similar emission signature to the blade coated films. Nonetheless, similarly to BA-1, the second broad band observed in **Figure 7b** also does not appear in the thin film PL of BA-2 in acetone. This observation leads us to conclude that similar effects to BA-1 solid are taking place in the BA-2 material.

Besides the difference in film quality, the acetonitrile thin film shows a second emission as intense as the excitonic one. This second band is very similar to the one observed in **Figure 7b**, but red shifted in 18 nm (609 to 627 nm). The most plausible hypothesis for this emission is a certain concentration of <n3> material, since the emission of this QW falls approximately in the same wavelength.[47] To further support

this idea, in the absorption of the **Figure 10c**, there is an absorption edge that matches with this second emission.

The PL decays rates of the powder BA-1, BA-2 and BLA-2 (**Figure 11**) agree with highly quantum-confined systems, given their fast radiative decay (See **Table 1**). For the BA-1 material, the PL decay rate is the same for both emissions (**Figure 11a**); therefore, a more plausible explanation for the lower energy emission at 545 nm is electron-phonon coupling, since, in general, this coupling occurs prior to emission. Again, whether it is electron-phonon coupling or the minibands from the overlap of the slabs wavefunctions, the degree of stacking must play an important role in this material.

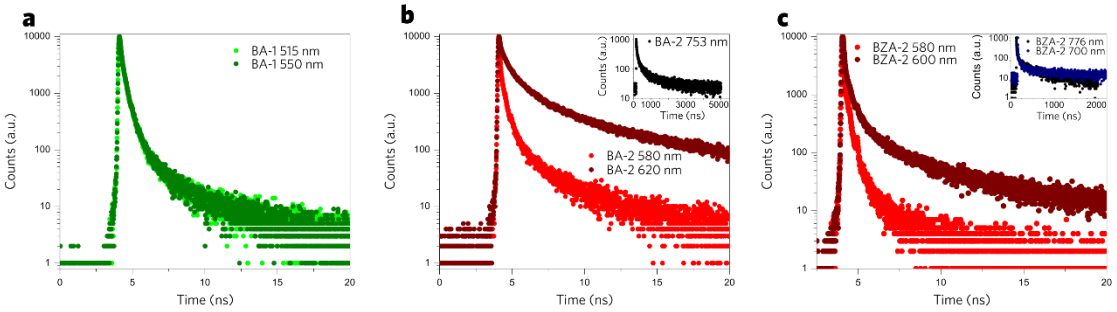

Figure 11. PL life time decay for the powder of the three materials in different emission maxima **a)** BA-1; **b)** BA-2; **c)** BLA-2.

In the case of *n*=2 materials, the first and the second bands are clearly distinct emissive states. Another phenomenon that can explain a split in the excitonic emissions is the free- and bound-excitons concept.[79] Emissions from free-excitons have virtually no Stokes-shift and come from excitons that decay as soon as they form. On the contrary, when excitons interact with defect states, they become bound emissive excitons (bound-excitons); since this emission is defect-assisted, its rate is larger. Therefore, for the BA-2 and BLA-2 powders, we probably observe both the free- and bound-excitonic emissions, as suggested by their different PL decay rate in **Figure 11b** and **11c**. For the emission decays at lower energies (>700 nm), the rates are consistent with STE process, as discussed before.[73] All the PL decay rates are summarized in the **Table 1**. All the decays were best fit with a triexponential equation. The values marked with an asterisk are omitted because the error of the measure is much larger than the measure itself (except for τ_2-BLA-2_{580}); the first component of the decay for all the materials is too fast and is beyond of the equipment detection limit.

Table 1. PL decay rates for the three RPLHPs powders in different emission wavelengths.

Sample	τ_1 (ns)	τ_2 (ns)	τ_3 (ns)	χ^2
BA-1_{515}	*	0.354 ± 0.090	1.395 ± 0.037	1.196
BA-1_{550}	*	0.335 ± 0.098	1.348 ± 0.034	1.309
BA-2_{580}	*	0.301 ± 0.155	1.427 ± 0.026	1.295
BA-2_{620}	*	0.871 ± 0.019	4.079 ± 0.004	1.294
BA-2_{750}	16.822 ± 0.004	138.618 ± 0.0003	994.012 ± 4.1E-5	1.075
BLA-2_{580}	*	0.157 ± 0.302	0.734 ± 0.073	1.569
BLA-2_{600}	*	0.609 ± 0.039	3.303 ± 0.008	1.176
BLA-2_{700}	3.008 ± 0.017	35.900 ± 0.002	773.934 ± 7.0E-5	1.075
BLA-2_{776}	4.135 ± 0.011	32.192 ± 0.002	347.405 ± 9.9E-5	1.088

In summary, RPLHPs present very complex and demanding spectral behaviors; although we could provide insightful explanations of their photophysics, further work must be carried out to precisely state their optical dynamics. In order to further investigate these materials, in the next section, we shall discuss a few more experiments probing their structure. We, then, sought to relate the insights gained from these experiments to what we have observed up to now.

3.5 - Structure to Properties Relationship

In order to verify what lies behind BA-2 PL behavior, we collected *in situ* grazing incidence wide angle X-ray scattering (GIWAXS) exposing the samples of BA-2 to white light (**Figure 12b**), UV-light (**Figure 12c**), and heat (**Figure 12d**). In general, the samples showed no difference in the diffraction patterns under any experimental conditions, revealing a surprising stability of the material (see **Figure 12a** for comparison). The only change is a continuous shift in the diffraction peaks as the temperature increases, associated to thermal dilatation of the crystal lattice, **Figure 12d**. Nonetheless, at temperatures above 170 °C, other diffractions evolve over time (**Figure 13**).

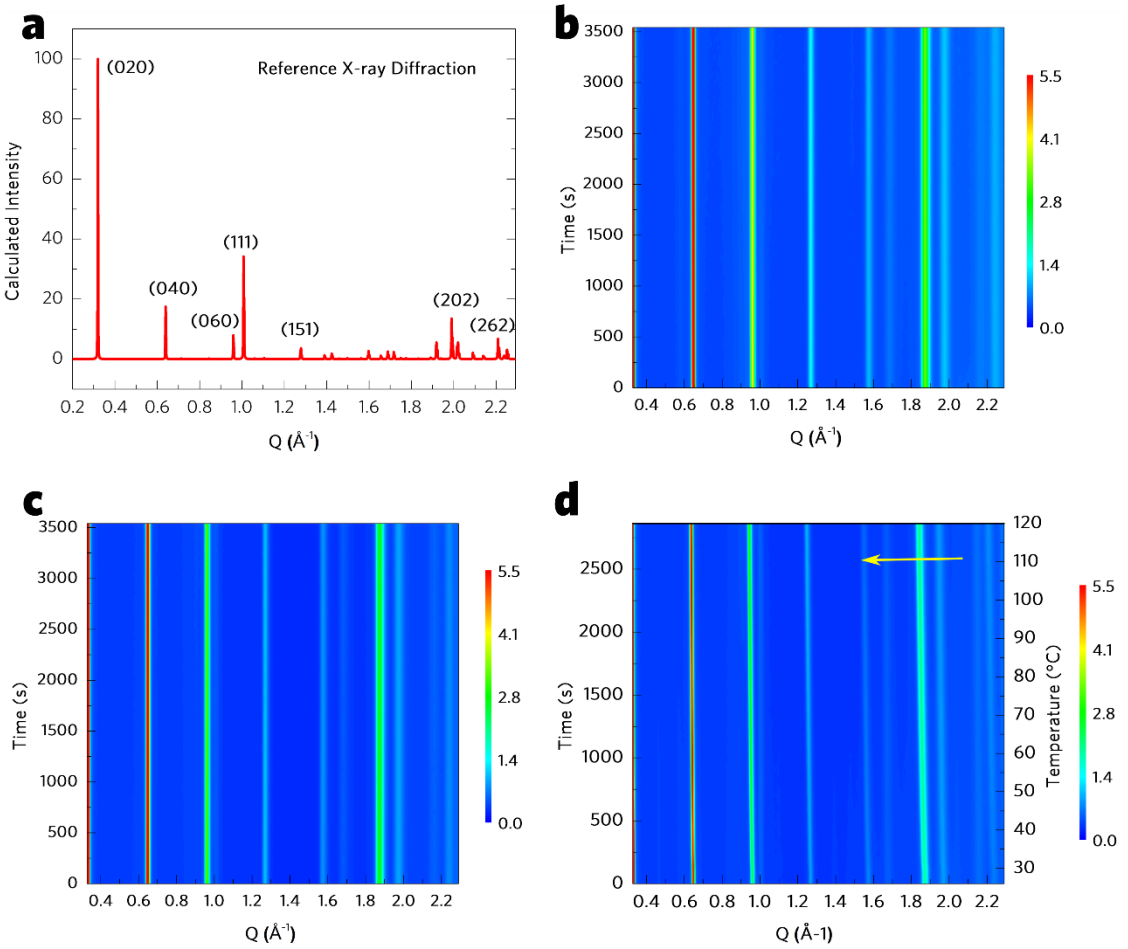

Figure 12. GIWAXS of the $BA_2[FAPbI_3]PbI_4$ solid **a)** reference XRD of the solid; **b)** in situ GIWAXS of the powder film under white light illumination; **c)** in situ GIWAXS of the film under UV light illumination (365 nm); **d)** in situ GIWAXS of the film varying the temperature – the arrow shows the direction of the peak-shifting.

Interestingly, besides no evidence of PbI_2 formation, it is unclear the presence of thicker QW phases. **Figure 13a** shows clearly that the peaks that arise as the sample is heated are Bragg reflections, and, from **Figure 13b**, we observe a few matching peaks with the phases <n2> and <n5>. However, we are still not able to precisely state the nature of the final material after this thermal treatment; furthermore, although the color of the film in the end of the reaction suggests that thicker QWs are being formed, we have no comparative data to verify phases with n>5, which limits the assignment of these emerging diffractions. Bulk $FAPbI_3$ perovskite should have an intense diffraction at approximately 1 $Å^{-1}$,[80] which is not the case. In addition, orientation with the temperature is also possible, which makes this interpretation even more difficult. Therefore, we conclude that, although the dark color of the film indicates a more bulk-like perovskite, the material is still a RPLHP, and the <n2> phase is apparently still present.

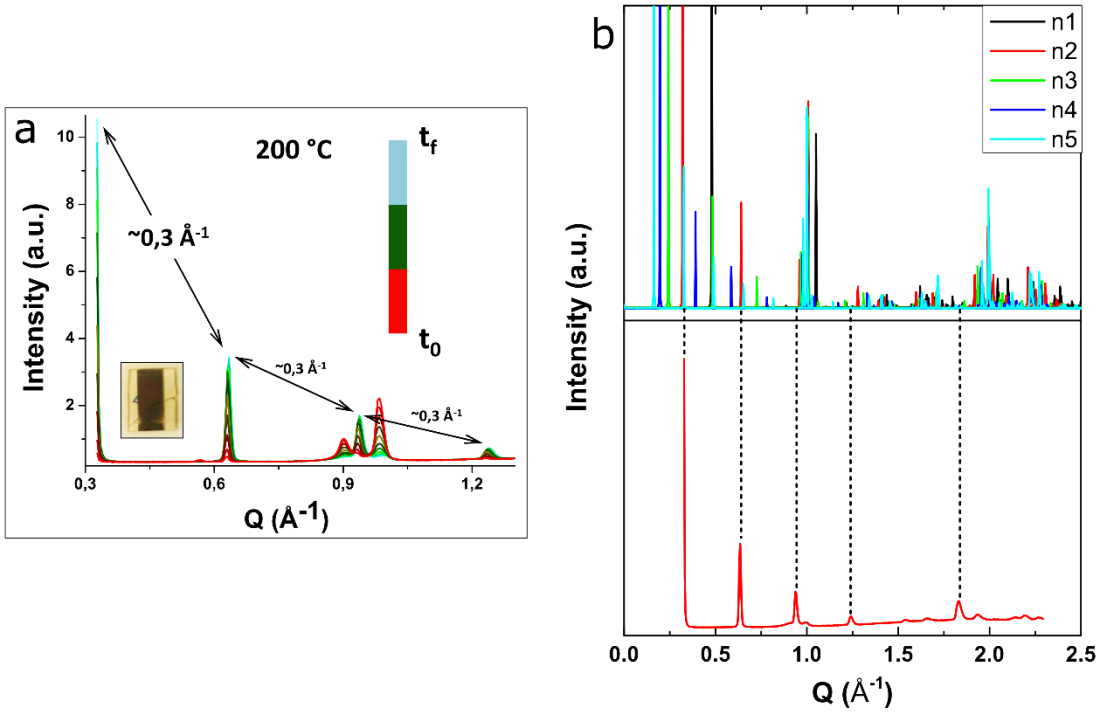

Figure 13. a) XRD evolution as the sample is heated at 200 °C for about 10 minutes - the insert is the sample after the experiment - and **b)** diffractograms from <n1> to <n5> compared to the last XRD collected from **a** – the dashed lines are only for visual guidance.

We expected that the *in situ* GIWAXS experiments could give us information on other QW phases, helping us understand better the optical signature of BA-2 material. However, we could only observe a rather surprising crystalline stability of this material, even under heat. This contrasting crystal stability and emission instability is the most intriguing and challenging feature of these materials. Nonetheless, an important conclusion from the GIWAXS experiments is that, within the temperature range we probed the samples, we could not observe any phase transition. This observation is particularly important to exclude the possibility of different polymorphs in the composition of the emission, which is the case of BA-1 at ~270 K.[49]

To verify the thermal stability of BA-2 and BLA-2 materials, we carried out thermogravimetric analysis (TGA) in both inert and oxidant atmosphere. The thermogravimetric curves are depicted in **Figure 14**. BA-2 material has a very clean and clear thermal decomposition under inert atmosphere (**Figure 14a**): the first mass variation of ~38% corresponds to the loss of all the organic molecules with equivalent amounts of HI, as described in the chemical reaction below:

$$BA_2[FAPbI_3]PbI_{4(s)} \rightarrow 2BA_{m(g)} + FA_{m(g)} + 3HI_{(g)} + PbI_{2(s)}$$

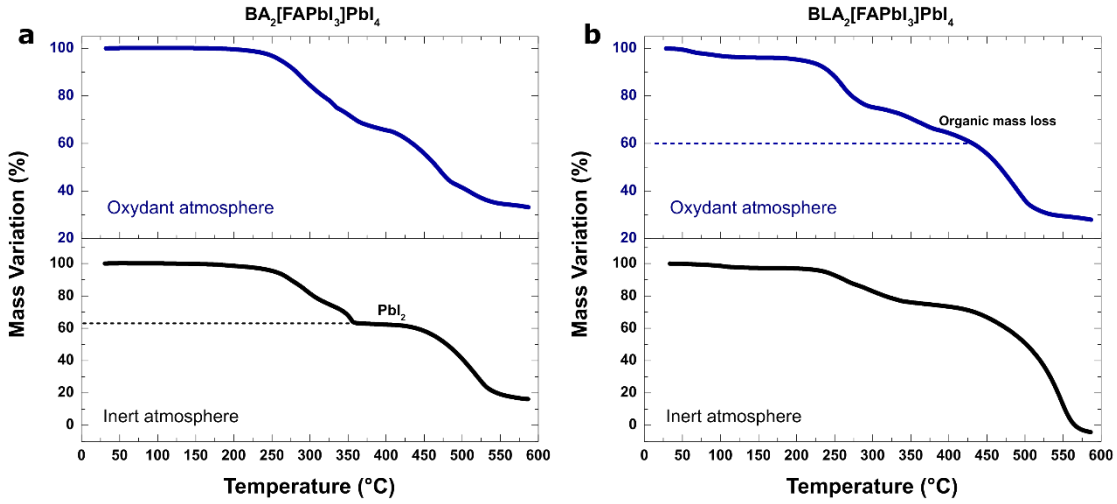

Figure 14. TGA analysis in both oxidant (blue curves) and inert (black curves) atmosphere. **a)** TGA curves of BA-2; and **b)** TGA curves of BLA-2. The dashed lines emphasize the loss events of the organic species.

where the subscript *m* in BA_m and FA_m denotes the respective deprotonated species (butylamine and formamidine). The sum of the masses of the organic molecules plus the three equivalents of HI correspond to 39% of the total molar mass of the BA-2 solid; the black curve in **Figure 14a** is, therefore, in great accordance with this prediction. Furthermore, TGA confirmed the incredible thermal stability of this material, as previously observed from the GIWAXS data.

The thermal decomposition of its benzylamine analogue, BLA-2, in inert atmosphere is not so clear. The total mass of organic species plus the equivalent amount of HI corresponds to 41% of the total molar mass of BLA-2; therefore, with a mass loss of 41%, we should expect to see a clear plateau corresponding to the remaining 59% in the black curve of **Figure 14b**, which is not the case. What we observe, though, is a first mass loss of ~3% right in the beginning, which is most likely from sample impurity, and a subsequent mass loss of ~24%. This 24% loss may be explained by the following chemical equation:

$$BLA_2[FAPbI_3]PbI_{4(s)} \rightarrow 2BLA_{m(g)} + 2HI_{(g)} + FAPbI_{3(s)}$$

where the subscript *m* has the same denotation than before, but for benzylamine. The sum of the masses of BLA_m and HI corresponds to 30% of the molar mass of BLA-2, which is considerably higher than the first loss event. These findings lead us to two suppositions: 1) BLA-2 material, even being prepared in a similar way of BA-2, seems to have some volatile impurities, as we addressed in the **Synthesis** section; and 2) this material may not

have the rigorous stoichiometry presented by its analogue BA-2. These assumptions explain the differences in the optical properties between these two materials and reinforce our initial suggestion that BLA-2 was more prone to form lattice defects.

The TGA of both materials in oxidant atmosphere are depicted in the blue curves in **Figure 14**. For BA-2, the oxidant thermal decomposition is similar to the inert analogue, but the loss events are overlapping. In the case of BLA-2, apparently, the loss of the organic species in oxidant atmosphere is clearer (dashed blue line); however, it is difficult to define precisely each loss event in oxidizing atmosphere, since oxygen mass is added to the material as the material thermally decomposes. In summary, TGA analysis confirmed the thermal stability of these materials and showed that their organic species are rather difficult to remove under heat.

As a final consideration, regarding the yellow material, BA-1, its PL spectrum presents no shift over time or under illumination. The PLE *vs* PL surface of this material is shown in the **Figure 15.** The important conclusion from **Figure 15** is that it indicates that both emissions come from the same energy states, as we discussed before; therefore, the hypothesis of electron-phonon coupling in this material seems to be the most plausible one. The fact that changes are not observable in BA-1 solid reinforces the idea of internal changes in the BA-2 and BLA-2 counterparts: since BA-1 cannot decompose into thicker QWs, because of the absence of FA^+ cations, this PL stability is expected. This yellow solid is quite stable under ambient atmosphere, and its green luminescence can be seen even after several months of exposure to ambient atmosphere (see inserted pictures in **Figure 15**). In fact, we have not observed any decomposition signal in BA-1 material at any point of this work.

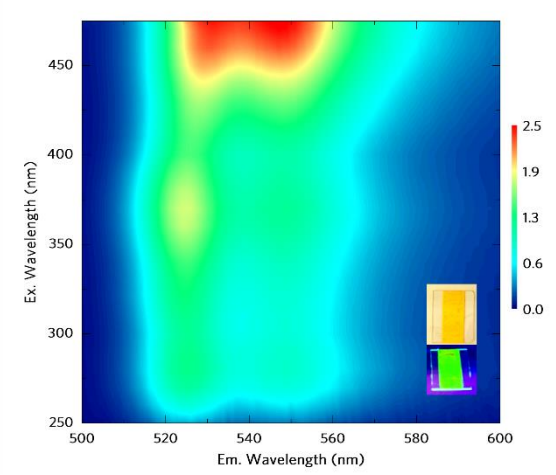

Figure 15. Optical properties of BA_2PbI_4 solid - PLE vs PL spectra on the film onto glass. The inserts are blade-coated films under UV light and ambient light onto glass substrate.

3.6 - Device Fabrication and Metrics

To demonstrate the applicability of these materials, we applied the BA-2 to a standard solar cell fabricated in our laboratory as a proof of concept. Very briefly, the red solid (BA-2) was fully dissolved in acetone and spin-coated onto a glass substrate. The solution of BA-2 is bright yellow, but it turns into the red RPLHP as soon as the solvent dries (**Figure 16 – left picture**). A thermal treatment was made in one of the devices, and the film became darker right away (**Figure 16 – right picture**). In general, only the cells with the thermal treatment worked well; the best devices parameters are depicted in **Table 2**. The general device configuration was FTO/TiO_2/BA_2[$FAPbI_3$]PbI_4/Spiro-OMeTAD/Au; where TiO_2 is the electron transporting material and Spiro-OMeTAD is the hole transporting material. The solar cells did not show an outstanding Power Conversion Efficiency (PCE) (**Table 2**), but they did show a photovoltaic behavior under biased potential, as can be seen in the curves of **Figure 16**.

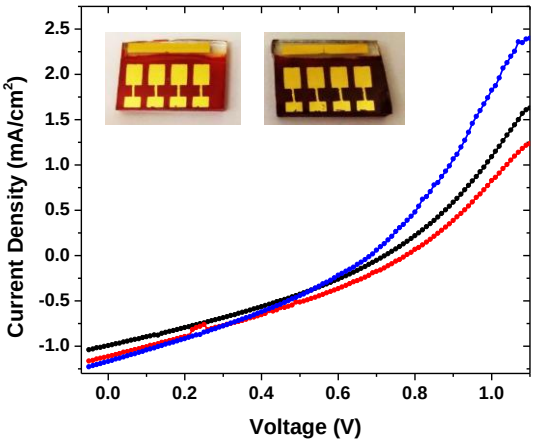

Figure 16. J-V curve for the solar cells together with the pictures of the devices – the darker film is the sample with thermal treatment.

Table 2. Solar cells metrics under 100 mW/cm^2 illumination power

Cell #	V_{oc} (V)	J_{sc} (mA/cm^2)	FF	PCE%
1	0.78	1.11	0.30	0.26
2	0.68	1.17	0.31	0.25
3	0.72	0.99	0.32	0.23
Average	0.73	1.09	0.31	0.25

The equations used to determine the parameters in **Table 2** are the following:[81]

$$Efficiency(PCE) = \frac{FF.V_{oc}.J_{sc}}{P_{solar}}$$

where the V_{oc} is the open circuit voltage (J = 0), J_{sc} is the current density when the potential is zero, P_{solar} is the solar power from the solar simulator, and FF is the fill factor, calculated by the following equation:

$$FF(\%) = \frac{V_{mp}.J_{mp}}{J_{sc}.V_{oc}}$$

where V_{mp} and J_{mp} are the potential and current at the maximum power point, respectively. All these parameters were extracted from the curves J-V in **Figure 16**; for detailed information, see the appendix for **Perovskite Solar Cells**.

It is worth mentioning that these devices did not have any optimization procedure such as the concentration of the BA-2 solution, optimal thermal treatment, spin-coating conditions, best solvent/method for film fabrication, etc. As thus, this 0.25% efficiency is just an initial achievement. In the next steps of this work, we must optimize the devices accordingly to obtain better outputs. We believe that, with this optimization, the efficiency of the solar cells can increase considerably.

BA-1 and BA-2 thin films were also used to fabricate porotype LEDs with configuration as follows: ITO/PDOT:PSS/PVK/BA-1 or -2/Ca/Al. Although the devices worked with applied potential (the LEDs blinked), calcium metal directly in contact with the RPLHP layer cause the material to degrade (*e.g.*, Ca reduces $Pb^{2+} \rightarrow Pb^0$ or $R\text{-}NH_3 \rightarrow R\text{-}NH_2 + H_2$). To avoid the use of calcium, other materials are adopted; a widely used strategy is the deposition of the electron-conducting polymer, TBPi.[61,82] Therefore, we believe that, in the next attempt, we will be able to fabricate functional LEDs, both with BA-1 and BA-2, by using other materials to replace calcium and optimizing fabrication conditions.

4 - Conclusion

We presented a new approach for the synthesis and processability of three different RPLHPs with ***n*** indexes of 1 and 2. This method, besides its simplicity and low-cost, allows the production of a paste-like ink, that can be directly used for film fabrication (*e.g.*, blade-coating, screen printing, etc.), or a dry powder for solution process methods (*e.g.*; spin-coating, deep-coating, etc.), which is desirable for optoelectronic applications. While traditional methods of perovskite deposition rely on meticulous solution preparation with several controlled measurements of mass and volume, solutions made directly from the powder compounds are particularly appealing because it guarantees stoichiometric precision and solution purity.

Although the BA-2 material showed incredible thermal and chemical resistance, its PL changes overtime, and its surface darkens. Similar effects are observed for BLA-2. We attributed these changes to the presence of other QW domains (although we could not detect them with XRD) and to lattice defects. Also, the broad emission feature, observed in both BA-2 and BLA-2, are most likely from STE, as largely discussed in the literature. However, this attribution is not yet conclusive, and more careful investigations are required for a precise assignment of these emission features.

We tested these materials in solar cells to have a proof of concept of their functionality and applicability. The devices presented a low PCE; however, we believe that, after a fine optimization, they might present improved efficiency. In addition, we also fabricated LEDs, applying BA-1 and BA-2 as the active layer, and obtained a positive response – the LEDs blinked under applied potential. The solar cells and LEDs outputs demonstrate the versatility and potential of the materials, and the results encourage us to future works.

Finally, this synthetic method is adaptable, allowing the use of other amines separators, other B-site metals, and other A-site cations. We believe that these materials can be functionalized with respect to the organic separating layer in ways that both domains synergistically interact (*e.g.*, introducing a fluorescent organic amine as a separator, charge extracting molecules, long chain primary diamines, etc.). Moreover, this synthesis has been tested with Cs^+ and other halides such as Br^- and Cl^-, and the resulting materials are similarly promising. As a final remark, we believe that this work opens a

new horizon for material design and provide new insights for the material science community.

5 – References

1 Sputnik: the fiftieth anniversary, https://history.nasa.gov/sputnik/, (accessed 2 January 2019).

2 PVEducation, https://www.pveducation.org/pvcdrom/introduction/introduction, (accessed 2 January 2019).

3 N. J. Jeon, J. H. Noh, Y. C. Kim, W. S. Yang, S. Ryu and S. Il Seok, *Nat. Mater.*, 2014, **13**, 897–903.

4 K. Yoshikawa, H. Kawasaki, W. Yoshida, T. Irie, K. Konishi, K. Nakano, T. Uto, D. Adachi, M. Kanematsu, H. Uzu and K. Yamamoto, *Nat. Energy*, 2017, **2**, 17032.

5 P.-J. Ribeyron, *Nat. Energy*, 2017, **2**, 17067.

6 J. Khan and M. H. Arsalan, *Renew. Sustain. Energy Rev.*, 2016, **55**, 414–425.

7 M. Saliba, J.-P. Correa-Baena, M. Grätzel, A. Hagfeldt and A. Abate, *Angew. Chemie Int. Ed.*, 2018, **57**, 2554–2569.

8 H. J. Snaith, *Nat. Mater.*, 2018, **17**, 372–376.

9 A. Kojima, K. Teshima, Y. Shirai and T. Miyasaka, *J. Am. Chem. Soc.*, 2009, **131**, 6050–6051.

10 H. S. Kim, C. R. Lee, J. H. Im, K. B. Lee, T. Moehl, A. Marchioro, S. J. Moon, R. Humphry-Baker, J. H. Yum, J. E. Moser, M. Grätzel and N. G. Park, *Sci. Rep.*, 2012, **2**, 1–7.

11 J. Burschka, N. Pellet, S.-J. Moon, R. Humphry-Baker, P. Gao, M. K. Nazeeruddin and M. Grätzel, *Nature*, 2013, **499**, 316–319.

12 *Nat. Mater.*, 2014, **13**, 837–837.

13 https://www.nrel.gov/pv/assets/pdfs/pv-efficiencies-07-17-2018.pdf, (accessed 14 September 2018).

14 H.-S. Kim, S. H. Im and N.-G. Park, *J. Phys. Chem. C*, 2014, **118**, 5615–5625.

15 P. Gratia, I. Zimmermann, P. Schouwink, J.-H. Yum, J.-N. Audinot, K. Sivula, T. Wirtz and M. K. Nazeeruddin, *ACS Energy Lett.*, 2017, **2**, 2686–2693.

16 Q. A. Akkerman, G. Rainò, M. V. Kovalenko and L. Manna, *Nat. Mater.*, 2018, **17**, 394–405.

17 L. Protesescu, S. Yakunin, S. Kumar, J. Bär, F. Bertolotti, N. Masciocchi, A. Guagliardi, M. Grotevent, I. Shorubalko, M. I. Bodnarchuk, C.-J. Shih and M. V. Kovalenko, *ACS*

Nano, 2017, **11**, 3119–3134.

18 C. Li, X. Lu, W. Ding, L. Feng, Y. Gao and Z. Guo, *Acta Crystallogr. Sect. B Struct. Sci.*, 2008, **64**, 702–707.

19 L. Protesescu, S. Yakunin, S. Kumar, J. Bär, F. Bertolotti, N. Masciocchi, A. Guagliardi, M. Grotevent, I. Shorubalko, M. I. Bodnarchuk, C. J. Shih and M. V. Kovalenko, *ACS Nano*, 2017, **11**, 3119–3134.

20 W. Travis, E. N. K. Glover, H. Bronstein, D. O. Scanlon and R. G. Palgrave, *Chem. Sci.*, 2016, **7**, 4548–4556.

21 W. Travis, E. N. K. Glover, H. Bronstein, D. O. Scanlon and R. G. Palgrave, *Chem. Sci.*, 2016, **7**, 4548–4556.

22 J. H. Noh, S. H. Im, J. H. Heo, T. N. Mandal and S. Il Seok, *Nano Lett.*, 2013, **13**, 1764–1769.

23 W. Shockley and H. J. Queisser, *J. Appl. Phys.*, 1961, **32**, 510–519.

24 J. H. Heo, S. H. Im, J. H. Noh, T. N. Mandal, C.-S. Lim, J. A. Chang, Y. H. Lee, H. Kim, A. Sarkar, M. K. Nazeeruddin, M. Grätzel and S. Il Seok, *Nat. Photonics*, 2013, **7**, 486–491.

25 S. D. Stranks, G. E. Eperon, G. Grancini, C. Menelaou, M. J. P. Alcocer, T. Leijtens, L. M. Herz, A. Petrozza and H. J. Snaith, *Science (80-.).*, 2013, **342**, 341–344.

26 G. Xing, N. Mathews, S. Sun, S. S. Lim, Y. M. Lam, M. Gratzel, S. Mhaisalkar and T. C. Sum, *Science (80-.).*, 2013, **342**, 344–347.

27 R. E. Powell, *J. Chem. Educ.*, 1968, **45**, 558.

28 F. Brivio, A. B. Walker and A. Walsh, *APL Mater.*, 2013, **1**, 042111.

29 B. Conings, J. Drijkoningen, N. Gauquelin, A. Babayigit, J. D'Haen, L. D'Olieslaeger, A. Ethirajan, J. Verbeeck, J. Manca, E. Mosconi, F. De Angelis and H.-G. Boyen, *Adv. Energy Mater.*, 2015, **5**, 1500477.

30 J.-W. Lee, D.-H. Kim, H.-S. Kim, S.-W. Seo, S. M. Cho and N.-G. Park, *Adv. Energy Mater.*, 2015, **5**, 1501310.

31 J. Yang, B. D. Siempelkamp, D. Liu and T. L. Kelly, *ACS Nano*, 2015, **9**, 1955–1963.

32 R. J. Sutton, G. E. Eperon, L. Miranda, E. S. Parrott, B. A. Kamino, J. B. Patel, M. T. Hörantner, M. B. Johnston, A. A. Haghighirad, D. T. Moore and H. J. Snaith, *Adv. Energy Mater.*, 2016, **6**, 1502458.

33 C. Yi, J. Luo, S. Meloni, A. Boziki, N. Ashari-Astani, C. Grätzel, S. M. Zakeeruddin, U. Röthlisberger and M. Grätzel, *Energy Environ. Sci.*, 2016, **9**, 656–662.

34 Q. Zeng, X. Zhang, X. Feng, S. Lu, Z. Chen, X. Yong, S. A. T. Redfern, H. Wei, H.

Wang, H. Shen, W. Zhang, W. Zheng, H. Zhang, J. S. Tse and B. Yang, *Adv. Mater.*, 2018, **30**, 1705393.

35 L. Zuo, H. Guo, D. W. DeQuilettes, S. Jariwala, N. De Marco, S. Dong, R. DeBlock, D. S. Ginger, B. Dunn, M. Wang and Y. Yang, *Sci. Adv.*, 2017, **3**, e1700106.

36 I. Hwang, I. Jeong, J. Lee, M. J. Ko and K. Yong, *ACS Appl. Mater. Interfaces*, 2015, **7**, 17330–17336.

37 Z. Zhu, D. Zhao, C.-C. Chueh, X. Shi, Z. Li and A. K. Y. Jen, *Joule*, 2018, **2**, 168–183.

38 Y. Zhang, J. Liu, Z. Wang, Y. Xue, Q. Ou, L. Polavarapu, J. Zheng, X. Qi and Q. Bao, *Chem. Commun.*, 2016, **52**, 13637–13655.

39 H. Tsai, W. Nie, J. C. Blancon, C. C. Stoumpos, R. Asadpour, B. Harutyunyan, A. J. Neukirch, R. Verduzco, J. J. Crochet, S. Tretiak, L. Pedesseau, J. Even, M. A. Alam, G. Gupta, J. Lou, P. M. Ajayan, M. J. Bedzyk, M. G. Kanatzidis and A. D. Mohite, *Nature*, 2016, **536**, 312–317.

40 J.-W. Lee, Z. Dai, T.-H. Han, C. Choi, S.-Y. Chang, S.-J. Lee, N. De Marco, H. Zhao, P. Sun, Y. Huang and Y. Yang, *Nat. Commun.*, 2018, **9**, 3021.

41 Y. Chen, Y. Sun, J. Peng, W. Zhang, X. Su, K. Zheng, T. Pullerits and Z. Liang, *Adv. Energy Mater.*, 2017, **7**, 1–7.

42 D. H. Cao, C. C. Stoumpos, T. Yokoyama, J. L. Logsdon, T.-B. Song, O. K. Farha, M. R. Wasielewski, J. T. Hupp and M. G. Kanatzidis, *ACS Energy Lett.*, 2017, 2, 982–990.

43 X. Zhang, R. Munir, Z. Xu, Y. Liu, H. Tsai, W. Nie, J. Li, T. Niu, D. M. Smilgies, M. G. Kanatzidis, A. D. Mohite, K. Zhao, A. Amassian and S. F. Liu, *Adv. Mater.*, 2018, **30**, 1–10.

44 K. T. Cho, Y. Zhang, S. Orlandi, M. Cavazzini, I. Zimmermann, A. Lesch, N. Tabet, G. Pozzi, G. Grancini and M. K. Nazeeruddin, *Nano Lett.*, 2018, **18**, 5467–5474.

45 S. N. Ruddlesden and P. Popper, *Acta Crystallogr.*, 1958, **11**, 54–55.

46 S. N. Ruddlesden and P. Popper, *Acta Crystallogr.*, 1957, **10**, 538–539.

47 C. C. Stoumpos, D. H. Cao, D. J. Clark, J. Young, J. M. Rondinelli, J. I. Jang, J. T. Hupp and M. G. Kanatzidis, *Chem. Mater.*, 2016, **28**, 2852–2867.

48 M. C. Weidman, M. Seitz, S. D. Stranks and W. A. Tisdale, *ACS Nano*, 2016, **10**, 7830–7839.

49 D. G. Billing and A. Lemmerer, *Acta Crystallogr. Sect. B Struct. Sci.*, 2007, **63**, 735–747.

50 G. A. Mousdis, G. C. Papavassiliou, C. P. Raptopoulou and A. Terzis, *J. Mater. Chem.*, 2000, **10**, 515–518.

51 K. Jemli, P. Audebert, L. Galmiche, G. Trippé-Allard, D. Garrot, J. S. Lauret and E. Deleporte, *ACS Appl. Mater. Interfaces*, 2015, **7**, 21763–21769.

52 L. Mao, W. Ke, L. Pedesseau, Y. Wu, C. Katan, J. Even, M. R. Wasielewski, C. C. Stoumpos and M. G. Kanatzidis, *J. Am. Chem. Soc.*, 2018, **140**, 3775–3783.

53 Y. Li, J. V. Milić, A. Ummadisingu, J.-Y. Seo, J.-H. Im, H.-S. Kim, Y. Liu, M. I. Dar, S. M. Zakeeruddin, P. Wang, A. Hagfeldt and M. Grätzel, *Nano Lett.*, 2018, acs.nanolett.8b03552.

54 D. B. Straus, S. Hurtado Parra, N. Iotov, J. Gebhardt, A. M. Rappe, J. E. Subotnik, J. M. Kikkawa and C. R. Kagan, *J. Am. Chem. Soc.*, 2016, **138**, 13798–13801.

55 J.-C. Blancon, H. Tsai, W. Nie, C. C. Stoumpos, L. Pedesseau, C. Katan, M. Kepenekian, C. M. M. Soe, K. Appavoo, M. Y. Sfeir, S. Tretiak, P. M. Ajayan, M. G. Kanatzidis, J. Even, J. J. Crochet and A. D. Mohite, *Science (80-.).*, 2017, **355**, 1288–1292.

56 D. B. Straus and C. R. Kagan, *J. Phys. Chem. Lett.*, 2018, **9**, 1434–1447.

57 V. K. Ravi, P. K. Santra, N. Joshi, J. Chugh, S. K. Singh, H. Rensmo, P. Ghosh and A. Nag, *J. Phys. Chem. Lett.*, 2017, **8**, 4988–4994.

58 A. H. Proppe, R. Quintero-Bermudez, H. Tan, O. Voznyy, S. O. Kelley and E. H. Sargent, *J. Am. Chem. Soc.*, 2018, **140**, 2890–2896.

59 G. Almeida, L. Goldoni, Q. Akkerman, Z. Dang, A. H. Khan, S. Marras, I. Moreels and L. Manna, *ACS Nano*, 2018, **12**, 1704–1711.

60 G. C. Papavassiliou3, G. A. M. Ousdis3, C. P. Raptopouloub and A. Terzisb, *Some New Luminescent Compounds Based on 4-MethyIbenzylamine and Lead Halides*, 2000, vol. 55.

61 Y. J. Yoon, K. T. Lee, T. K. Lee, S. H. Kim, Y. S. Shin, B. Walker, S. Y. Park, J. Heo, J. Lee, S. K. Kwak, G.-H. Kim and J. Y. Kim, *Joule*, 2018, **2**, 2105–2116.

62 J. De Roo, M. Ibáñez, P. Geiregat, G. Nedelcu, W. Walravens, J. Maes, J. C. Martins, I. Van Driessche, M. V Kovalenko and Z. Hens, *ACS Nano*, 2016, **10**, 2071–2081.

63 R. M. (Robert M. Silverstein, F. X. Webster, D. J. Kiemle and D. L. (David L. Bryce, *Spectrometric identification of organic compounds*, Wiley, 8th edn., 2014.

64 D. Roy, G. F. Samu, M. K. Hossain, C. Janáky and K. Rajeshwar, *Catal. Today*, 2018, **300**, 136–144.

65 J. B. Coulter and D. P. Birnie, *Phys. status solidi*, 2018, **255**, 1700393.

66 B. Brunetti, C. Cavallo, A. Ciccioli, G. Gigli and A. Latini, *Sci. Rep.*, 2016, **6**, 31896.

67 G. Xing, B. Wu, X. Wu, M. Li, B. Du, Q. Wei, J. Guo, E. K. L. Yeow, T. C. Sum and W. Huang, *Nat. Commun.*, 2017, **8**, 14558.

68 Y. Fu, W. Zheng, X. Wang, M. P. Hautzinger, D. Pan, L. Dang, J. C. Wright, A. Pan and S. Jin, *J. Am. Chem. Soc.*, 2018, **140**, 15675–15683.

69 E. R. Dohner, A. Jaffe, L. R. Bradshaw and H. I. Karunadasa, *J. Am. Chem. Soc.*, 2014, **136**, 13154–13157.

70 K. Thirumal, W. K. Chong, W. Xie, R. Ganguly, S. K. Muduli, M. Sherburne, M. Asta, S. Mhaisalkar, T. C. Sum, H. Sen Soo and N. Mathews, *Chem. Mater.*, 2017, **29**, 3947–3953.

71 T. Hu, M. D. Smith, E. R. Dohner, M.-J. Sher, X. Wu, M. T. Trinh, A. Fisher, J. Corbett, X.-Y. Zhu, H. I. Karunadasa and A. M. Lindenberg, *J. Phys. Chem. Lett.*, 2016, **7**, 2258–2263.

72 A. Yangui, D. Garrot, J. S. Lauret, A. Lusson, G. Bouchez, E. Deleporte, S. Pillet, E. E. Bendeif, M. Castro, S. Triki, Y. Abid and K. Boukheddaden, *J. Phys. Chem. C*, 2015, **119**, 23638–23647.

73 O. Nazarenko, M. R. Kotyrba, S. Yakunin, M. Wörle, B. M. Benin, G. Rainò, F. Krumeich, M. Kepenekian, J. Even, C. Katan and M. V. Kovalenko, *Chem. Mater.*, 2019, **31**, 2121–2129.

74 M. E. Kamminga, H.-H. Fang, M. R. Filip, F. Giustino, J. Baas, G. R. Blake, M. A. Loi and T. T. M. Palstra, *Chem. Mater.*, 2016, **28**, 4554–4562.

75 D. B. Mitzi, *Chem. Mater.*, 1996, **8**, 791–800.

76 J. B. Birks, *Reports Prog. Phys.*, 1975, **38**, 903–974.

77 J. A. Sichert, Y. Tong, N. Mutz, M. Vollmer, S. Fischer, K. Z. Milowska, R. García Cortadella, B. Nickel, C. Cardenas-Daw, J. K. Stolarczyk, A. S. Urban and J. Feldmann, *Nano Lett.*, 2015, **15**, 6521–6527.

78 J. Even, L. Pedesseau and C. Katan, *ChemPhysChem*, 2014, **15**, 3733–3741.

79 M. D. Smith, B. A. Connor and H. I. Karunadasa, *Chem. Rev.*, 2019, **119**, 3104–3139.

80 R. Quintero-Bermudez, A. Gold-Parker, A. H. Proppe, R. Munir, Z. Yang, S. O. Kelley, A. Amassian, M. F. Toney and E. H. Sargent, *Nat. Mater.*, 2018, **17**, 900–907.

81 H. Yu, S. Zhang, H. Zhao, G. Will and P. Liu, *Electrochim. Acta*, 2009, **54**, 1319–1324.

82 P. Vashishtha, M. Ng, S. B. Shivarudraiah and J. E. Halpert, *Chem. Mater.*, 2019, **31**, 83–89.

83 L. Boldon, F. Laliberte and L. Liu, *Nano Rev.*, 2015, **6**, 25661.

84 O. Glatter and O. Kratky, *Small angle x-ray scattering*, Academic Press, 1982.

85 B. R. Pauw, *J. Phys. Condens. Matter*, 2014, **26**, 239501.

6 – Appendix

6.1 – Appendix Figures

Appendix Figure 2. BA-2 blade-coated films prepared with a paste of the solid in toluene.

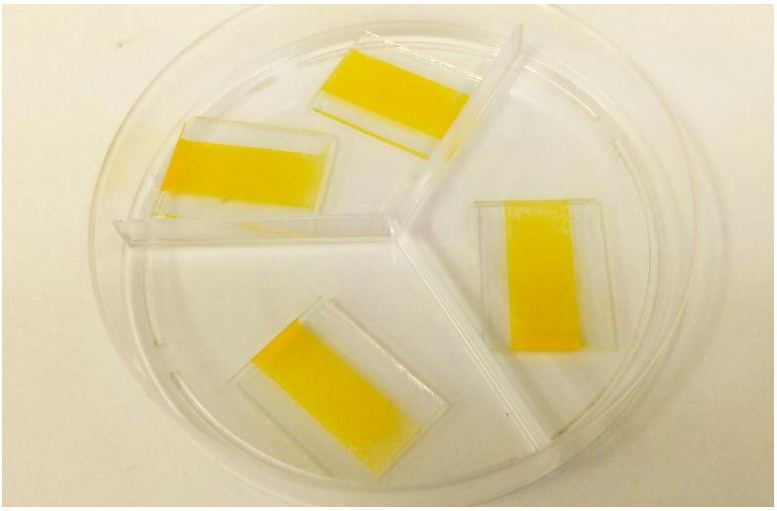

Appendix Figure 1. BA-1 blade-coated films prepared with a paste of the solid in toluene.

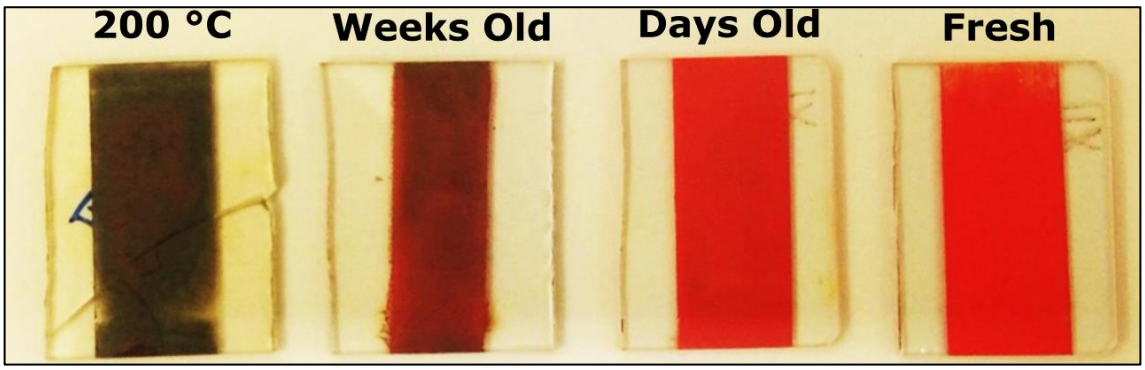

Appendix Figure 3. Different levels of darkening of the $BA_2[FAPbI_3]PbI_4$ films – the leftmost was thermally treated at 200 °C for a couple of minutes; the three remaining ones, from right to left, were exposed to air and normal light for different periods of time.

6.2 - Small angle X-ray Scattering and (Gazing Incidence) Wide Angle X-ray Scattering: a Brief Overview

In simple words, SAXS is a technic that relies on the X-ray scattering from particles of ~1 nm to over a few hundred nanometers;[83] and (GI)WAXS relies on the diffraction from adjacent crystalline planes, just like normal X-ray diffraction. There is no well-defined limit between the regimes of X-ray scattering and X-ray diffraction. In general, SAXS data are collected in a range of the scattering vector, Q, from 10^{-1} to 10^{0} $Å^{-1}$, whereas (GI)WAXS data are usually detected beyond 10^{0} $Å^{-1}$. The relationship between Q and θ° is found in the **Equation 1**:

$$\lambda = \frac{4\pi.sen\theta}{Q} = 2d.sen\theta \longrightarrow Q = \frac{2\pi}{d}$$

Equation 1. Relationship between the Q vector and the Bragg's law (θ).

The convenience of the Q vector is that it does not depend on the energy of the incident beam. As before mentioned, the border of SAXS and (GI)WAXS regimes are not well-defined and depend on the material being studied. This feature had special importance in the discussion of this work, when a diffraction peak was detected in "SAXS regime".

The scattering in small angles works as a microscope: since the constructive overlap of waves scattered from large particles tends to 0°, the smaller the particle, the wider the constructive scattering angle, which makes SAXS a technic suitable to investigate nanometric systems.[84] This fact is better understood in the scheme below:

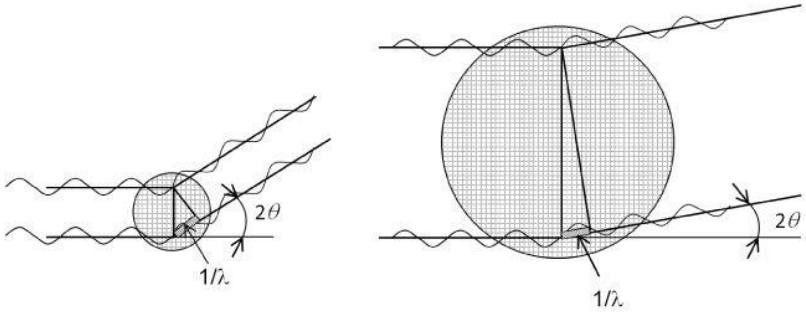

Appendix Scheme 1. The small and large scattering particles example – image from nmi3.eu (accessed on 04/06/18).

The intensity of the scattering curve depends on the square of the electron density difference between phases in the sample; that is, the larger the electron density contrast, the larger the scattering contribution. Without electron density contrast there is no SAXS signal. For the scattering curves, one must find the best fitting model within the experimental errors and extract information about the system such as size, shape, mass, or even the electron density. It is true because the theoretical scattering intensity of a particle depends on the scattering amplitude, the electron density contrast, and the volume of the particle.[83] However, collecting this set of information can be a very difficult task and often depends on supporting technics/models such as TEM and molecular dynamics calculations.

The amplitude of scattering is a function of the electron density of the material ρ(r), given by the integration over the volume of the particle; for a sphere, we have:

$$A_{sphere}(q) = \int_V \rho(r) e^{-iqr}\, dr$$

The form factor function, P(q), depends, obviously, on the morphology of the particle. For a sphere:

$$P_{sphere}(q) = \frac{A_{sphere}(q)^2}{V_p}$$

where V_p is the volume of the sphere. Similarly, P(q) for a cylinder:

$$P_{cyl}(q) = \left[\int_0^1 A_{cyl}(q) * 2sin\alpha . d\alpha\right]^2$$

where α is the angle between the z axis (X-ray beam axis) and Q. The scattering intensity of a single particle is then given by:

$$I_p(q) = A(q)A(q)^* = (\Delta\rho)^2 V_p^2 P(q)$$

where Δρ is the electron density contrast of the system.

Hence, for a population of particles, we have:

$$I(q) = \sum_{i=1}^{n} I_{p_i}(q)$$

For a monodisperse population given by the distribution d(r) below

$$d(r) = \frac{1}{\rho\sqrt{2\pi}} exp\left[-\frac{(r-R)^2}{2\sigma^2}\right]$$

The profile of the scattering intensity is then obtained by:

$$I(q) = \sum_{i=1}^{n} d_i(r) I_{p_i}(q)$$

A weighted normalized summation of the populations is carried out in case of polydisperse systems. These equations may be directly used for spherical, cylinder, or disk models.[83,85]

6.3 – Perovskite Solar Cells

A perovskite solar cell (PSC) is a device capable of converting electromagnetic radiation into electricity. The basic working principle of these devices is quite simple: light induces the formation of electron hole pairs in a semiconductor material; if enough time is given to the absorber, these pairs will recombine. In order to produce electrical work, this absorber must be between materials capable of extracting these charge carriers separately; that is, electrons are collected in one side, while hole are conducted to the opposite side. Hence, the electrons will pass through an external circuit, produce electrical work, and finally recombine with the holes on the anode. A schematic PSC is depicted in the figure below:

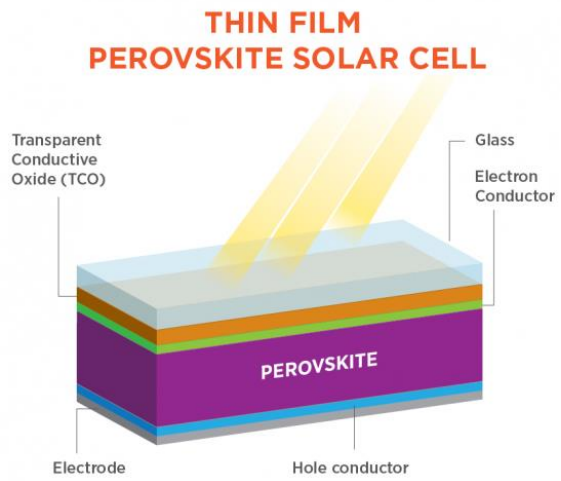

Appendix Scheme 2. A typical perovskite solar cell. Image taken from https://www.energy.gov/eere/solar/perovskite-solar-cells (accessed on April 18, 2019).

The performance of a solar cell is measured by evaluating the current that the device produces per unit of active area under a bias potential (*i.e.*, a potential applied opposing the cell potential). From this curve, we extract information such as the FF and the PCE of the devices, as discussed in section 3.5. The FF is a measure of the quality of the device: the closer it gets from unit, the better is the device performance. A typical plot of current density *vs* potential (J-V curve), from where the FF is calculated, is depicted bellow:

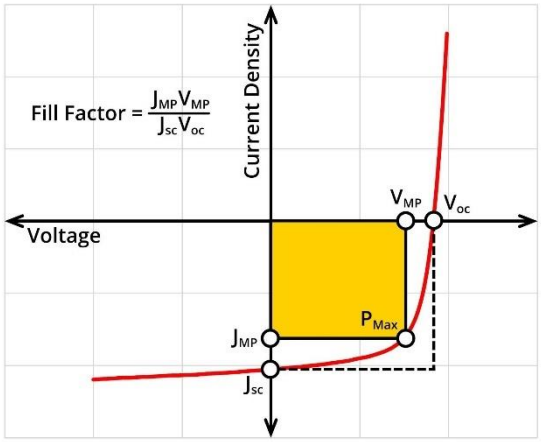

Appendix Scheme 3. Typical J-V curve to evaluate a solar cell performance. Image taken from https://www.ossila.com/pages/solar-cells-theory (accessed on April 18, 2019).